Doctoral Dissertations and Master's Theses

Spring 2023

The Role of Slip System Activation on Ni-Based Superalloy High Temperature Fatigue

Alexandru Lopazan
Embry-Riddle Aeronautical University, lopazana@my.erau.edu

Follow this and additional works at: https://commons.erau.edu/edt

Part of the Structures and Materials Commons

By

A Thesis Submitted to the Faculty of Embry-Riddle Aeronautical University

In Partial Fulfillment of the Requirements for the Degree of

Master of Science in Aerospace Engineering

Embry-Riddle Aeronautical University

Daytona Beach, Florida

By

THESIS COMMITTEE

_____   _____

_____   _____

_____   _____
Graduate Program Coordinator,   Date
Dr. Hever Moncayo

_____   _____
Dean of the College of Engineering,   Date
Dr. James W. Gregory

_____   _____
Associate Provost of Academic Support,   Date
Dr. Christopher Grant

To my parents and my sister, for giving me the chance to be where I am today.

ACKNOWLEDGEMENTS

I would like to thank Dr. Alberto Mello for his guidance as my thesis advisor and his time as my professor in both the undergraduate and graduate program. I would also like to thank Dr. Sirish Namilae and Dr. Daewon Kim as my committee members. Thank you to all the professors and faculty I have had who have taken the time to teach me, work with me, and make me a better engineer. Thank you to all my friends and classmates who have made my time at university even more enjoyable. Finally, I want to especially thank my family members for always supporting in me and believing in me.

ABSTRACT

Nickel-based superalloys are used extensively in the aviation industry, particularly in aircraft engine components. These materials are desirable due to their high strength, resistance to creep, corrosive environment, and high temperature. It has been well documented that material fatigue is characterized by material microstructure, type of loading, and other parameters. Currently, research into the effects of fatigue on complex materials like nickel-based superalloys is being pursued. Previous research has found that preconditioning of Inconel 718 samples at 700 °C with 1.0% strain led to an improved fatigue life. It has been suggested that this could be caused by the activation of the {100} cubic slip plane along the usual {111} octahedral slip plane. This study continued the work of previous research by using SEM and EBSD imaging to characterize the microstructure of IN-718 specimens before and after preconditioning. The microstructure grains and their orientations before preconditioning were found for a distinct area of interest using EBSD. Following the preconditioning, the same study area was found and activity inside the grains were monitored. Following preconditioning, some grains exhibited bidirectional slip bands while others exhibit unidirectional. Characterizing these slip bands showed that some resided in the {111} system while others, particularly the bidirectional slip bands, resided in the {100} direction. This confirms that the preconditioning caused the activation of the cubic slip system. As such, this favorable change in the microstructural better accommodates the applied stress and reduces the strain localization, leading to the improved fatigue life. Future research can be conducted in-situ by using a special frame and heater inside the microscope chamber. This will allow monitoring engineering strain and slip band formations as heat and load are applied. Such equipment is not available at the moment, but is part of the equipment development proposal of the ERAU Aerospace Material Research Group.

TABLE OF CONTENTS

LIST OF FIGURES

LIST OF TABLES

NOMENCLATURE

Variables

A Material property to be determined for Basquin's Law

a_o Initial Crack Size

B Material property to be determined for Basquin's Law

b Material property to be determined for Coffin-Manson Equation

c Material property to be determined for Coffin-Manson Equation

E Young's Modulus

K Stress Intensity Factor

K_{RZ} Rough Zone Stress Intensity Factor

l_{gb} Initial crack tip

N Number of Cycles

N_f Number of Cycles until failure

R Stress Ratio

S, σ Stress

α Crack angle, Primary Crystal Orientation

β Secondary Crystal Orientation

σ_a Amplitude Stress

σ_{ar} Unnotched Amplitude Stress

σ_{bo} Friction stress

σ_m Mean Stress

σ_u Ultimate Stress

$\sigma_f{}'$ Fatigue Strength Coefficient

ε	Strain
ε_a	Summation of elastic and plastic strain
$\varepsilon_f{}'$	Fatigue Ductility Coefficient
$\varDelta\varepsilon_t$	Total Strain Amplitude

Abbreviations

AM	Additive Manufacturing
AOI	Area of Interest
BCC	Body Centered Cubic
CO	Crystal Orientation
DIC	Digital Image Correlation
DT	Damage Tolerance
EBSD	Electron Backscatter Diffraction
EDX	Energy-Dispersive X-ray
ERAU	Embry-Riddle Aeronautical University
FCC	Face Centered Cubic
HCF	High Cycle Fatigue
IPA	Isopropyl Alcohol
LCF	Low Cycle Fatigue
NDI	Non-Destructive Inspection
OA	Over-aging
OA2	Two-stage aging
ON	Orientation Number
OM	Optical Microscope

PSB   Persistent Slip Bands

SEM   Scanning Electron Microscope

TEM   Transmission Electron Microscope

TWIP   Twinning-Induced Plasticity

UA   Under-aging

UFG   Ultrafine Grained

VHCF   Very High Cycle Fatigue

1. Introduction

In the aerospace industry, a major focus on developing new, more specialized materials has been at the forefront of research and testing. As aircraft and spacecraft become increasingly more complex, the demand for components that can withstand the rigors of operation has increased drastically. The requirements of newer materials depend largely around properties such as durability in hostile environments (high temperatures, corrosion, vacuum), increased strength while reducing weight, and active materials that can fit a number of complex roles. As such, the development of improved Superalloys has been a recent topic of research. The objective of this research is to corroborate and find an explanation for the findings of the work done by Mello et al. [1] and De La Torre and Mello [2] in their focus on Superalloys and how strain preconditioning led to an increase in material fatigue life. The goal is to determine if the improvement in fatigue life is due to preconditioning causing favorable microstructural changes that better resist applied stress.

1.1 Importance of Research

The focus of this research is driven by the importance of two main topics: material fatigue and superalloy materials. This section will discuss these topics and why they are important in the aviation industry. The remainder of the paper will discuss the relation of these two topics to each other.

1.1.1 Material Fatigue

Fundamentally, fatigue can be described as a structural response within the material to loading. The effects of fatigue are primarily caused by the structure undergoing cyclic loading. The first thought when considering failure in a structure is that the cause most likely is attributed to the structural loading having exceeded ultimate load. However, it is rare for this overloading to occur in normal operation. As an example, from the aviation industry, the operation of an aircraft is

1

inherently considered cyclic in nature. At a smaller, structural specific scale, cyclic forces such as vibrational loads and phenomenon such as flutter occur within the structure. However, it is a combination of the usual loads that an aircraft experiences during its mission profile and its operational life that has the greatest influence on structural fatigue. Examining the standard mission profile of an airliner, the main segments are Taxiing, Take-off, Climb, Cruise, Descent, and Landing. The airliner's structure and all its components experience unique loadings that are specific to each of the mentioned stages. These loads are taken into consideration during the design process to ensure that the structures can withstand them. However, in the normal operational life of any aircraft, their mission is performed hundreds if not thousands of times depending on the aircraft and its role. This essentially defines the flight profile as a cycle loading problem as all the loads associated throughout the stages of a mission profile are now experienced repetitively. While specific occurrences such as vibrations do have an effect on component fatigue, it is the cyclic loading from an aircraft's mission profile over its operational life that is the primary defining factor.

The main risk that fatigue presents within a material is the cracking formation. The existence of cracks is described by three stages. These three stages are crack nucleation, crack initiation, and crack propagation. Crack nucleation can be summarized as when the initial location of the crack is defined. The defining factor of this stage is pre-existing material defects, such as cell vacancies known as dislocations. The cyclic loading that the structure experiences and the stresses associated with them leads to dislocation movements, accumulation of the vacancies in a weak spot of the material causing an initial defect. While at this stage the risk point in the material is not yet a crack, it is considered a nucleation and is an example of strain localization, because of all the internal movements within the grain. As the material continues experiencing the cyclic loading that caused

2

nucleation, the next stage of crack initiation is reached. It is because of those stresses that the initial separation at the nucleation point continues to become more severe and then forms the crack itself. Once the crack has been initiated, the final stage of crack propagation is reached. As in the previous stages, the continual application of cyclic loading leads to the growth of the crack. In general, the magnitude, frequency, and loading order of the cyclic loads defines the severity of the crack growth rate.

These three stages explain why there is a high risk of failure due to fatigue. Exceeding a material's ultimate load is fundamentally avoidable during normal operation. However, it is an aircraft's normal operation that leads to the structure experiencing cyclic loading which is the cause of cracking. This makes it clear that the formation and propagation of cracks within the structure is likely to occur during an aircraft's operational life. It is the continued growth of a crack that causes material failure as once a critical crack size is reached, the component will break. Some other major factors that can also influence the initiation process and the severity of the crack growth rate are the material microstructure, environment, and operating temperature.

Due to the risk that fatigue poses to an aircraft structure, it is important to be able to account for crack growth to ensure the critical crack size is never reached. This is what led to the establishment of Damage Tolerance (DT), Non-Destructive Inspection (NDI), and other maintenance requirements and regulations. At this point the mathematics that define fatigue and crack growth is well known and allows the crack growth to be defined in number of cycles that the aircraft experiences. One of the most fundamental equations is Basquin's Law (1.1) [3]. Where σ_a is stress amplitude, N_f is number of cycles, and A and B are material properties based on a log-log fitting of stress-life cycle test data. This equation is fundamental to the Stress-life (S-N) method of predicting fatigue life when the material is elastic, which is reflected on a S-N curve as seen in

Figure 2.1. However, to predict fatigue life more accurately, mean stress (σ_m) of the loading cycles need to be accounted for. That is where equations such as Goodman's (1.2), Soderberg, Morrow, Gerber, Walker (1970), and others come into play [3]. Below is Goodman's equation, one of the most used equations that account for mean stress, where σ_{ar} is amplitude stress of unnotched components and σ_u is the material ultimate stress. By taking mean stress into account and correcting all loadings to have a mean of zero, the Palmgren-Miner Rule [3] (1.3) can be used to determine total damage and number of cycles of loading before failure, where N_j is number of cycles for a loading and N_{f_j} is the cycles to failure for a loading. The multitude of equations available allow for many methods of determining fatigue life of a structure. However, beyond the S-N method there is also the Strain-life (ε-N) method of fatigue life prediction which is used when the material reaches plastic deformation. A common equation associated with the ε-N method is the Coffin-Manson equation (1.4) [3] where E is the elastic modulus, σ_f' is fatigue strength coefficient and ε_f' is the fatigue ductility coefficient, b and c are material properties, and ε_a is the summation of elastic and plastic strain.

$$\sigma_a = AN_f^B \tag{1.1}$$

$$\frac{\sigma_a}{\sigma_{ar}} + \frac{\sigma_m}{\sigma_u} = 1 \tag{1.2}$$

$$\sum_j \frac{N_j}{N_{f_j}} = 1 \tag{1.3}$$

$$\varepsilon_a = \frac{\sigma_f'}{E}\left(2N_f\right)^b + \varepsilon_f'\left(2N_f\right)^c \tag{1.4}$$
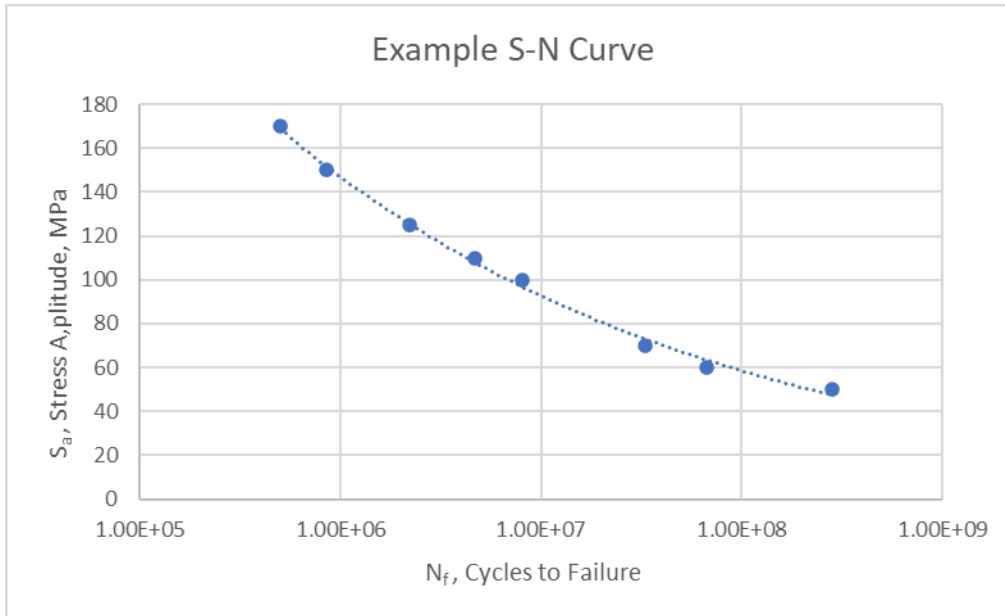
Figure 1.1: Typical S-n curve and how environment affects fatigue life.

1.1.2 Slip Mechanisms

While fatigue as a concept has been covered overall, it is important to understand the role that slip mechanisms play in material fatigue. Every material in some way has microstructural defects and voids – absences of atoms within the microstructure. Collectively, these defects can be called dislocations [3], essentially any irregularity within the microstructure that changes the arrangement of atoms abruptly. Due to these dislocations within the structure, when the material experiences loading, some dislocations can displace relative to the rest of the microstructure. The movement of the dislocations occur along close-packed planes which are known as slip planes. In the case of Face Centered Cubic (FCC) crystals, the common slip plane is the octahedral plane {111} [3] as seen in Figure 1.2.
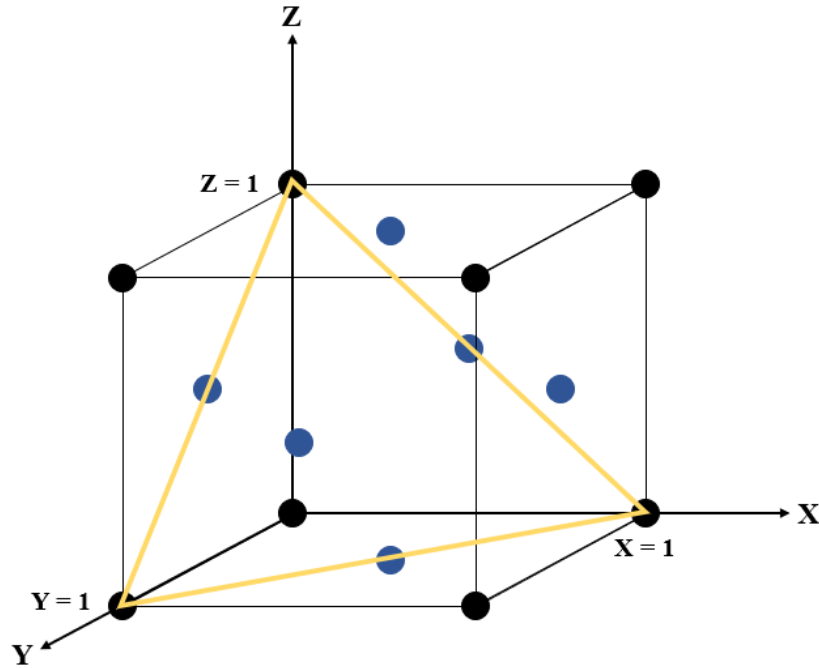
Figure 1.2: Graphic of FCC Crystal with {111} plane highlighted.

As the microstructure experiences continued loading and begins to experience slip, localized areas of plastic deformation known as slip bands might form [3]. Their formation is likely caused by a consistent unidirectional slip in a given slip plane of the structure. While these bands do not grow beyond grain boundaries, the risk they pose is the stress concentration that occurs in the bands. Eventually, the stress concentration (or rather strain localization) and fatigue leads to Persistent Slip Bands (PSBs) [3]. As was discussed in the previous section, strain localization is the primary cause of crack nucleation and eventual crack growth. From this, slip bands are an ideal indicator to characterize how cyclic stress acts on the microstructure and causes fatigue effects.

1.1.3 Superalloys

As mentioned earlier, the desire for new and more complex materials has increased as the aviation industry grows. This is what led to the discovery of superalloys [4]. In particular, as propulsion technology in the aviation industry began to become more advanced, the needs for a material that was able to counter restricting factors such as high temperature operation, creep, and

vibrational loads [5]. In response to this restriction, the studying of new materials and combination of different metals around 1930 lead to the discovery of the γ' phase. The γ' phase can be described as alloy percipitate that causes the strengthening of the alloy [4]. When Inconel-718 was developed, the γ'' phase was discovered which represents a percipitate that acts as the main strengthening factor in the Iconel. By adjusting the kinds of materials added into the alloy, the strengthening of the material could be increased. In this time frame, nickel and cobalt began to be used in the alloys along with more common materials like aluminum and titanium. What was established in this time is that the way to define superalloys is by their microstructure, chemical composition, and plane constitution. The solid phases (like γ') are what define the microstructure of the material and cause the improved mechanical qualities that are desired from superalloys [4]. It was the continued development of jet engine technology that pushed the study and advancement of superalloys to become more widespread in the 1940s. Intriguingly, in the 1950s and 1960s, researchers began combining more materials leading to over-alloying. A result of this was the discovery of the σ phase and the effects of the μ and Laves phase that was found in the 1930s. These phases, unlike the γ' phase, are brittle and detrimental to the superalloy. By the 1980s, the over-alloying was reduced as researchers focused on using fewer materials that ensure that the superalloy has desired characteristics. By this point, the knowledge of these phases are well known and are being used to make the most desirable superalloys.

From the discoveries made about them, superalloys were able to be classified by the main material found within the superalloy matrix (γ), which by this point are commonly nickel, cobalt, or iron-nickel [6] and then further defined by other materials that were used to augment the properties of the alloy. In the case of nickel and cobalt based alloys, it was discovered that another phase that constituted the microstructure where the Carbides MC, M_6C, and $M_{23}C_6$. The structures

of the phases that have been discussed can be seen in Table 1.1. Each phase has their own characteristics and have unique effects on the characteristics of the superalloy they constitute. [4, 7].

Table 1.1: Common nickel-based superalloy phases.

Phase	Structure	Appearance	Result
γ	Austenitic FCC	General background	Fundamental structural support of material
γ'	Simple FCC cubic	Variable (cubes, spheres, etc.)	Primary strengthener of material
γ''	Two FCC cubes stacked	Small disks	Main strengthener in Inconel-718
Carbide	FCC	Strings of beads	Dispersion strengthening, improving grain bonding
σ	TCP	Long, brittle plates	Poor mechanical properties
μ	TCP	Long, brittle plates	Poor mechanical properties
Laves	TCP	Short rods	Poor mechanical properties

Particularly important to this paper, nickel-based superalloys have their own characteristics that make them desirable for certain applications. Following much research and development of the nickel-based superalloys since the 1930s, it was detemined that this alloy was capable of withstanding high temperatures. [4] At most, the nickel-based superalloys are able to tolerate temperatures as high as 1200 °C (roughly 70% of the melting temperature) which has made them ideal for standard operation at temperatures at or above ~500 °C. At this temperature, many common metals and some alloys will have already reached their melting point. Along with the resistance to high temperatures, it was also studied that superalloys exhibit desireable toughness, resistance to corrosive environments, and a resistance to creep at high temperatures. These properties have led to these specific superalloys to find much useage in the propulsion units of aircraft and even some other areas such as rocket propulsion or energy processing plants [8]. The ability of these materials to resist high temperatures and maintain their strength is why they are

8

used in many aircraft engine components. In fact, it has been studied that superalloys account for about 50% of an aircraft engine's total weight, with that number potentially increasing as the superalloys become more specialized [9]. Some of the components that use superalloys include turbine blades, engine shafts, afterburners, thrust reversers, combustion chamber, and other components of the engine that experience sustained high temperatures during operation. In particular, Inconel-718 has been used in roughly 34% of all superalloys used in the engine and primarily is used in the combustor and turbine regions. It is clear that the advancement of propulsions systems and superalloy materials occurred hand in hand [9] .

1.2 Importance of Fatigue and Superalloys

The preceeding subsections provide the background for what material fatigue is and the history and explanation of superalloys. As mentioned before, the effects of fatigue and the eventual crack growth associated with is considered inevitable. With the risk that crack growth poses to a structure, particularly an aircraft, it is essential for designers to be aware of these effects and how to predict fatigue life and account for it during the design phase. As for superalloys, their importance in the aviation industry has been well realized. In general, these materials are more difficult to develop and come at a higher cost than more common materials such as aluminum and steel. However, the benefits that the superalloys bring to a structure because of their desirable characteristics is undoubtedly worth the cost. Understanding the phases of the superalloys is important when developing new specialized superalloys that can meet the demands of the aviation industry as it advances. Building on this, it is also important to understand how fatigue relates to superalloys. This is the driving idea for this research of understanding and potentially improving the fatigue life of nickel-based superalloys based on the material microstructure. Being able to study and improve the fatigue life of newer more complex materials is paramount if the use of these materials becomes ubiquitous in aviation.

2. Review of the Relevant Literature

This section will review existing literature that involves the main concepts that are influential to the research of this paper. The literature that will be discussed is separated into three areas of focus: dislocation effects, nickel-based superalloy fatigue, and other related topics. The purpose of this is to examine what research and findings have already occurred to be able to draw a logical conclusion from the results of the present work.

2.1 Main References

This first section will focus on the two primary papers that represent the work done before the present research. The results and implications of both papers will be discussed to provide an understanding of what is driving the research conducted in this paper.

As mentioned before, the work conducted in this research was a direct continuation of the work conducted by De La Torre and Mello [2]. That study was also an expansion of the findings of Mello et al. in their 2017 paper titled "Fatigue strain mapping via image correlation for Ni-based superalloys: The role of thermal activation on cube slip" [1]. The purpose of this paper was to investigate strain deformation mapping as it is affected by temperature, applied strain, and number of cycles. Understanding Mello et al.'s usage of SEM, EBSD, and Digital Image Correlation (DIC) to study material microstructure was essential for understanding the work done in the present research.

As covered earlier and discussed by Mello et al. [1], strain localization within the material is the main factor that leads to eventual crack initiation. It is addressed that plastic deformation of the material is attributed by microstructural slip occurring and that thermal activation causes this slip to occur below the mechanical threshold as addressed in this paper's introduction. Based on the effect slip and temperature have on the plasticity of the material, Mello et al. [1] used SEM, EBSD, and DIC to characterize the material slip variable to temperature, strain, and cycle number

of a proprietary nickel-based superalloy CG RR1000. The testing temperatures used were 300 ℃ (low), 550 ℃ (intermediate), and 700 ℃ (high). The testing cycles used were 1, 10, 100, and 1000 cycles and the applied strain amplitudes were 0.7% (low) and 1.0% (high). By interrupting the fatigue testing on the samples at varying testing conditions, the slip bands were found and compared using DIC.

Good examples of the DIC results that relate to the present research are Figures 2.1 and 2.2. Figure 2.1 shows the evolution of the slip bands at the varying test conditions at an initial strain amplitude of 0.7%. Figure 2.2 shows the same evolutions but at an initial strain amplitude of 1.0%. Mello et al. explain that the expectations of the fatigue experimentation are that increasing cycles would lead to an increase in the slip activity of the material. In the case of the 0.7% strain (Figure 2.1), it is shown that the slip activity does increase for all testing temperatures up until strain saturation is reached. At 300 ℃ the strain continued to increase beyond 1000 cycles. However, Mello et al. observed that for 550 ℃ and 700 ℃, strain saturation occurs between 100 and 1000 cycles and 1 and 10 cycles respectively. In comparison, the results of the fatigue testing at 1.0% (Figure 2.2) strain amplitude had some minor and major differences. With regards to the testing conducted at 300 ℃, it is clear from Figure 2.2 that there is higher strain localization occurring in the 1 to 10 cycle stage than at 0.7% strain. By the 1000 cycle, the strain activity continued to increase. At 550 ℃, the strain saturation that occurred in between cycles 100 and 1000 at 0.7% strain happened between cycles 1 and 10 for 1.0% strain. Logically this would occur due to the higher strain level being applied to the microstructure. The most interesting difference between the two strain evolutions is that at 700 ℃ for 1.0% strain there was seemingly no change in the evolution between 1 and 100 cycles and minimal change beyond that.
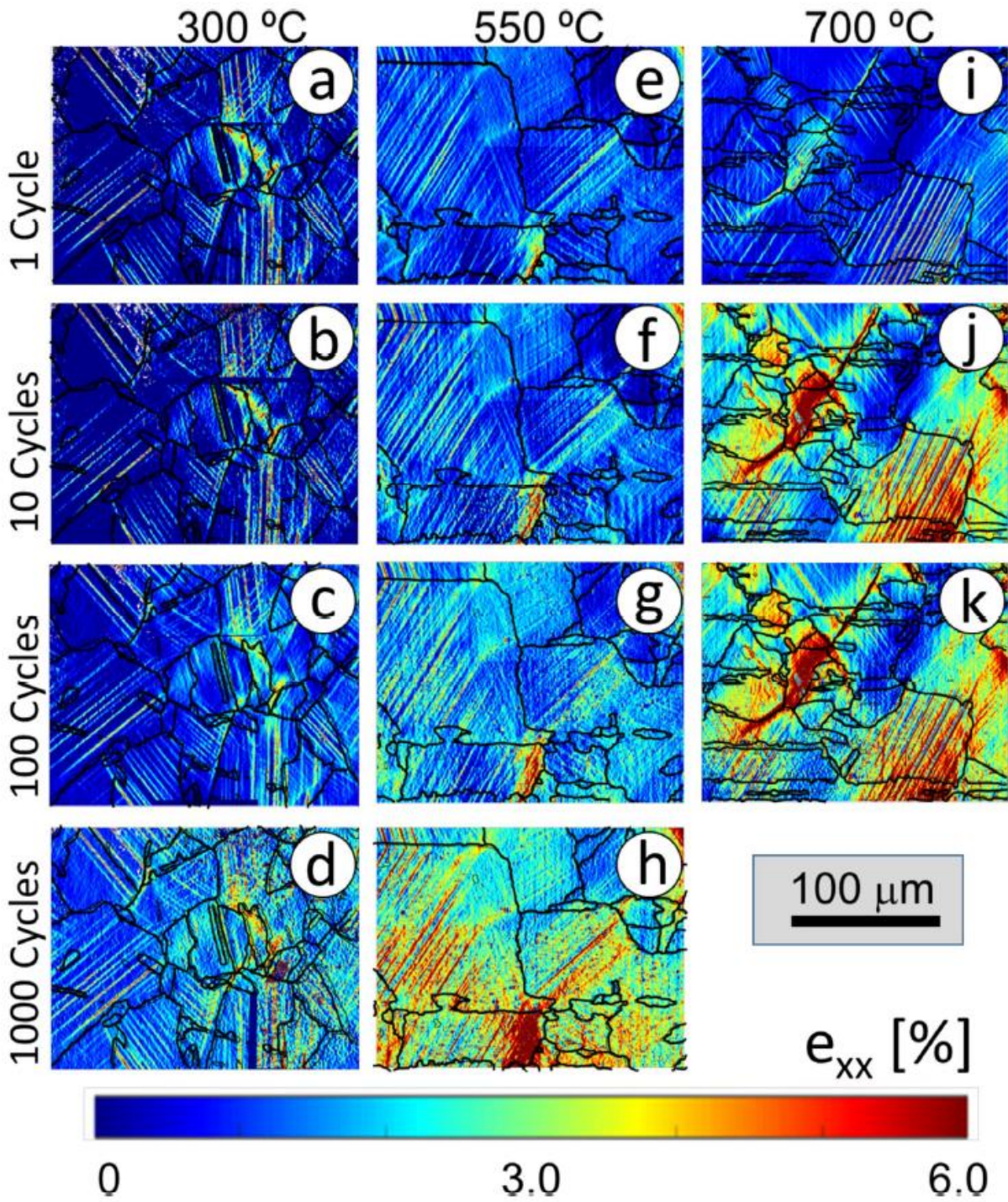
Figure 2.1: Strain evolution for CG RR1000 specimens at 300 °C, 550 °C, and 700 °C mapped at 1, 10, 100, and 1000 cycles, loaded to 0.7% initial strain. [1]
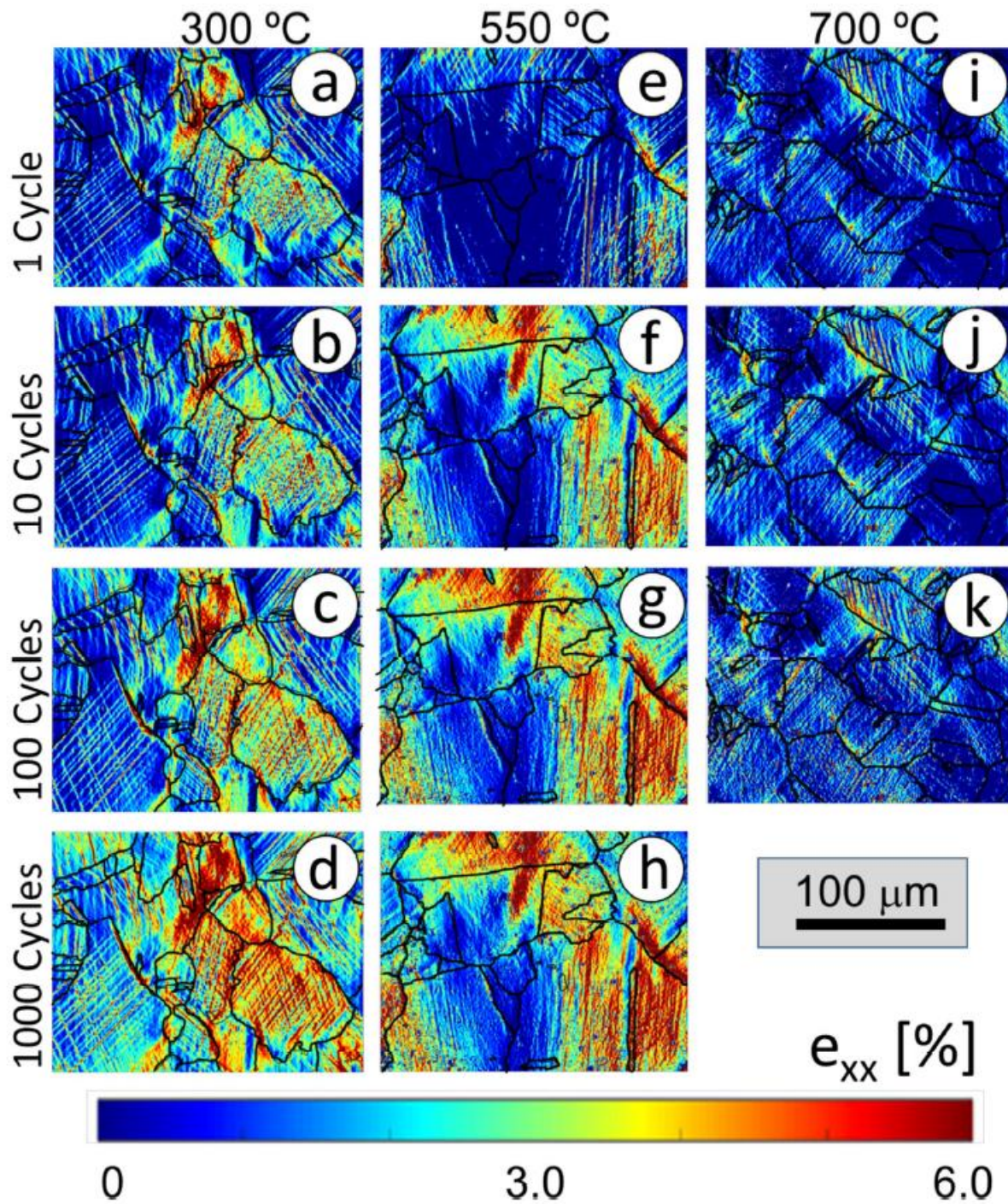
Figure 2.2: Strain evolution for CG RR1000 specimens at 300 °C, 550 °C, and 700 °C mapped at 1, 10, 100, and 1000 cycles, loaded to 1.0% initial strain. [1]

The other conclusions reached by Mello et al. following the experimentation are discussed below. From the strain mapping, it is evident that the deformation behaves in planar directions.

From the different segments of testing, it was found that at 300 °C, the octahedral slip plane {111} was active, and all deformation occurred there regardless of strain. In contrast, at 700 °C the cubic slip plane {100} was also active, causing the deformation to be accommodated in both slip systems. In the case of 550 °C, at 0.7% strain only the {111} slip plane was active and at 1.0% strain a smaller amount of {100} slip plane was activated as well [1]. This is shown in Figure 2.3. Mello et al. explain that following the first cycles of loading, the slip bands are formed. However, as the cycles continued, it was observed that no new slip bands formed and the distances between the bands also stayed the same.
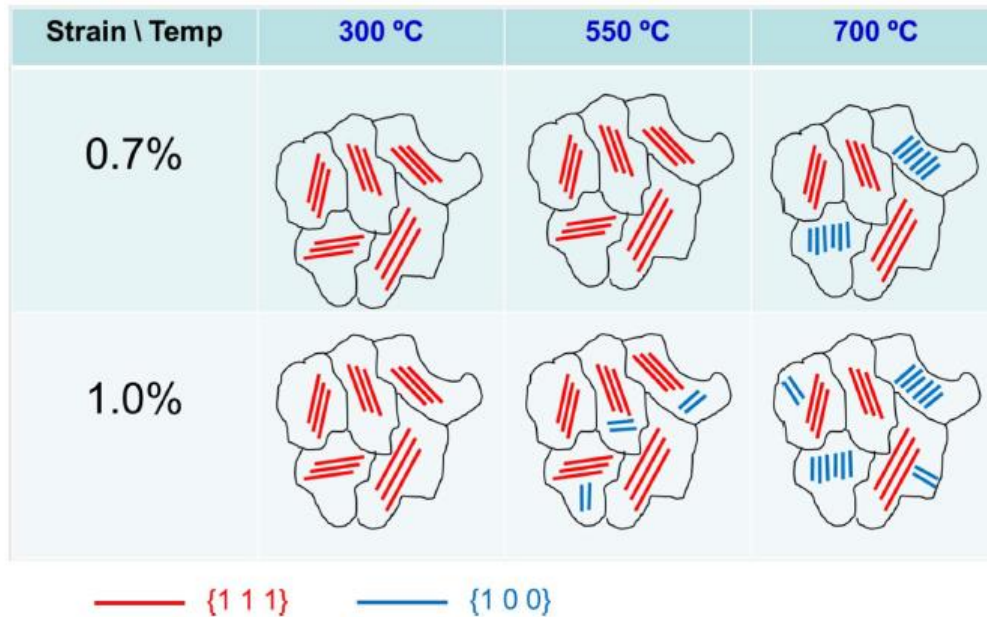
Figure 2.3: Evolution of octahedral and cubic slip system activation as a function of temperature and macroscopic applied strain. [1]

Mello et al. [1] make it clear that the results of the 1.0% strain at 700 °C experiment implied an important effect on the fatigue life of nickel-based superalloys. The key finding from the strain mapping is that the higher temperature caused a thermal activation of the cubic slip plane alongside the octahedral slip plane. Mello et al. [1] describe that because of this, more strain could be accommodated in the bands and in more favorable directions within the microstructure. This

14

allows strain saturation to occur in distinct regions. This finding and its implication of improving superalloy fatigue life is the seed for the research done by De La Torre [2].

Fundamentally, the work done by De La Torre and Mello in their paper "The effect of pre-thermal and -load conditions on IN-718 high temperature fatigue life" is based on the findings from Mello et al. [1] regarding the increased strain accommodation at higher temperature and strain loading accommodation. The goal of this study is to verify that the activation of both the octahedral {111} and cubic {100} slip planes due to thermal activation and its effect on superalloy fatigue life.

De La Torre's investigation depended on conducting monotonic and fatigue testing on Inconel 718 samples. Samples 1 and 2 underwent monotonic testing so the stress-strain curve of the Inconel could be characterized. For sample 1, the test was conducted at room temperature and the yield stress (σ_{ys}) and Youngs modulus (E) were found to be 1020 MPa and 198 GPa. For sample 2, the test was conducted at 700 °C with a resulting σ_{ys} and E of 867 MPa and 193 GPa. Samples 3 and 4 were used as control samples for the fatigue testing. Essentially, the purpose was to determine what was the general fatigue life of the Inconel samples. For both samples, the testing temperature was 500 °C with σ_{max} of 636 MPa and σ_{min} of 64 MPa to have a Stress Ratio (R) of 0.1. The difference between the two tests was that sample 3 had a frequency of 0.5 Hz and sample 4 had a frequency of 1.0 Hz. The resulting fatigue life of samples 3 and 4 was 24729 and 28159 cycles, respectively. Finally, sample 5 was where material preconditioning was applied. The preconditioning (also can be considered an overloading) was done at 700 °C, at a σ_{max} of 884 MPa and σ_{min} of 0 MPa for one cycle. A 1-minute dwell time was conducted once the maximum stressed was reached to allow the microstructure to settle from its adjustment. Following the

unloading and cooling of the sample, a fatigue test was conducted with the same parameters as was done for sample 4 until fracture.

The result of this preconditioned sample fatigue test was that the fatigue life was found to be 111361 cycles. This fatigue life is nearly four times greater than that of the unconditioned Inconel samples. According to De La Torre, this result supports the hypothesis that high strain and high temperature preconditioning would reduce the effect of strain localization. This seemingly validates the findings of Mello et al. [1].

2.2 Dislocation Effects

The focus of this section is reviewing literature that involves the role that dislocation slip plays on crack growth within a microstructure. What is important to note in these reports is that they do not focus strictly on nickel-based superalloy, but rather on dislocation slip plays a role in other materials and understanding how it affects fatigue. Understanding its role in other materials can be beneficial in understanding better its effects in the present research. While there are many more papers on this subject, the ones presented in this section are discussed to provide their unique insight on the overarching subject matter.

The first paper is by Z.J. Zhang et al. titled "Effects of dislocation slip mode on high-cycle fatigue behaviors of ultrafine-grained Cu-Zn alloy processed by equal-channel angular pressing" [10]. Zhang et al. explain that ultrafine-grained (UFG) materials have shown much promise with their great mechanical properties as discussed by Singh et al. [11], however their fatigue properties have not been well studied at that point. In the case of UFG Cu, a wavy-slip material, studies of purity and refinement methods showed that not much improvement of its fatigue limit could happen. In comparison, it is discussed how UFG Mg, Ti, and α Cu-Zn alloys, which are planar-slip materials, have improved fatigue limits. Zhang et al. surmise that the type of slip mode of a UFG material has a large effect on the material's fatigue life. To further study this, Zhang et al.

16

used two Cu-Zn alloys with separate alloy percentages and subjected them to High Cycle Fatigue (HCF) testing using an INSTRON 8871 fatigue testing machine at room temperature. These were also compared fatigue testing of only UFG Cu. In all cases, two specimens were tested undergoing equal-channel angular pressing for 1 pass and 4 passes, respectively. Before and after the testing, both a SEM and a transmission electron microscope (TEM) were used to characterize and compare the alloys' microstructure. From the experimentation of the Cu-11 at. % Zn and Cu-5 at. % Zn alloys, Zhang et al. determine that increasing the Zn content causes the dislocation cross-slip to be restricted, strain localization was better confined, and the fatigue life was improved by a large margin. Overall, it appeared that the alloyed materials had a better fatigue life than the Cu samples. They further conclude that adjusting or confining dislocation slip mode is the key to improving fatigue life and that alloying is an effective method to do so. Images of fatigue damage for the different samples can be seen in Figure 2.4. While this paper focuses on UFG materials, it addresses the importance of alloying and slip adjustment.
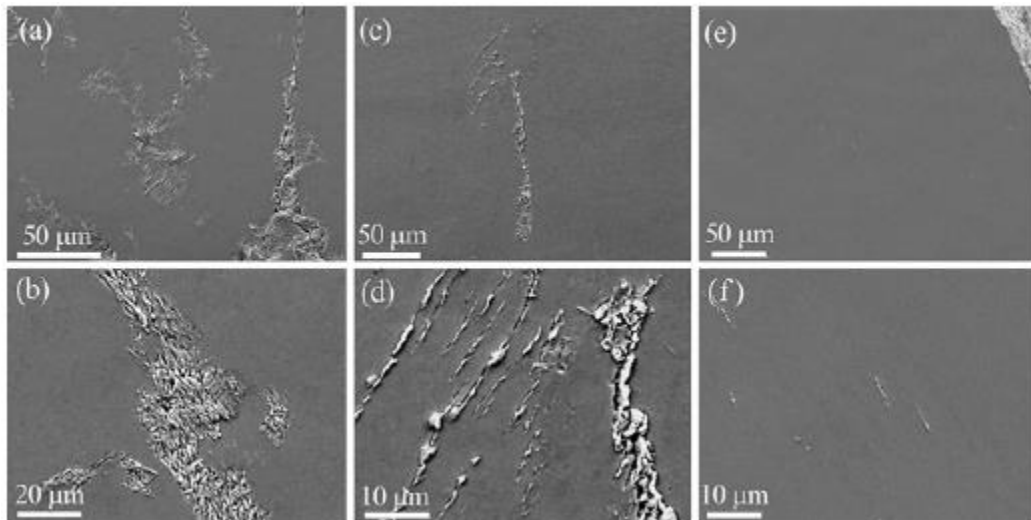

Figure 2.4: Fatigue damage morphologies of the sample after ECAP for four passes: (a) and (b) Cu: $\Delta\sigma2 = 160$ MPa, 1.1×10^6 cycles; (c) and (d) Cu-5 at.% Zn: $\Delta\sigma2 = 180$ MPa, 2.5×10^5 cycles; (e) and (f) Cu-11 at.% Zn: $\Delta\sigma2 = 220$ MPa, 7.3×10^5 cycles. [10]

Continuing with these concepts, the paper "Effects of Al₃Sc particle size and precipitate-free zones on fatigue behavior and dislocation structure of an aged Al-Mg-Sc alloy" by Watanabe et al [12] examines particle size effects on fatigue. In a previous study by them, it was found that aged Al-Mg-Sc specimens with sizes of 4 nm and 11 nm, with dispersed spherical Al₃Sc each exhibited unique fatigue behaviors. The 4 nm alloy experienced cyclic softening while the 11 nm experiences cyclic hardening. In this paper, Watanabe et al. investigate the dislocation structure by fatigue testing Al-Mg-Sc alloys under multiple constant amplitude strains. For their testing, Watanabe et al. subjected sets of specimens to each of the following aging processes: under-aging (UA) at 573 K for 9.0×10^2 s, over-aging (OA) at 623 K for 6.48×10^4 s, and two-stage aging (OA2) at 573 K for 3.0×10^2 s, water quenched and then at 623 K for 6.48×10^4 s. The resulting Al₃Sc particle size was 4 nm for under-aging and 11 nm for over-aging and two-stage aging. The specimens were then fatigue tested using a ramp method starting a 0.5 Hz for 30 cycles and increasing up to 10 Hz every tens of cycles. Following the fatigue testing, Watanabe et al. prepared their samples and used a TEM to observe the microstructure. Their findings reiterated the pattern that smaller particles of 4 nm experienced cyclic softening while larger particles of 11 nm experienced cyclic hardening. More importantly, it was observed that in the small-particle specimens, the formation of slip bands was observed. Watanabe et al. make it clear that the cause of the material softening is due to the Al₃Sc particles partially re-dissolving within the slip bands and not due to surface cracks. In the case of the large-particle specimens, the dislocations were uniformly distributed within the microstructure, so the fatigue life was improved. Finally, the two-step aging specimens had an improved fatigue life due to a decrease in the size of precipitate-free zones. The resulting S-N curve of the different aging method specimens by Watanabe et al. can be seen below in Figure 2.5.

This study reinforces the role the microstructure and the varying sizes of particles within it plays a role in dislocation/slip effects.
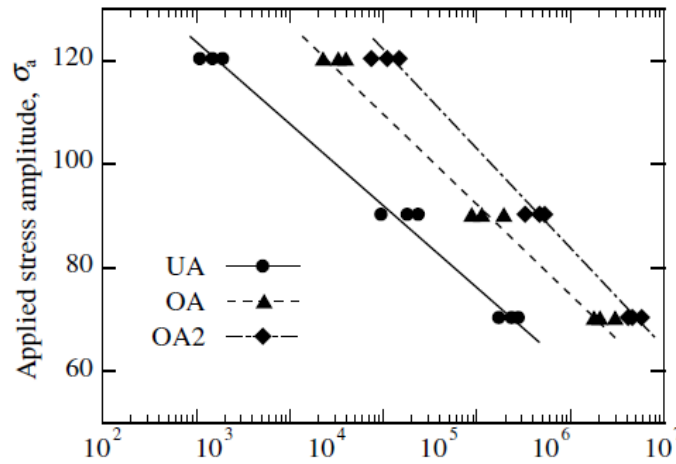
Figure 2.5: Number of cycles to failure, N_f. [12]

Finally for the papers involving dislocation effects, there is the paper by Hansson and Melin titled "Dislocation-based modelling of the growth of a microstructurally short crack by single shear due to fatigue loading" [13]. This study is unique compared to the previous two papers as their work did not involve working with physical specimens and testing devices. Hansson and Melin, understanding the roles that crack growth and fatigue plays on the life of a structure, in this paper discuss how they created a dislocation-based model to analyze potential crack growth within a material based on the work by Bjerkén and Melin [14]. The focus of their model is determining crack paths, crack shapes, plastic zone, and crack opening in a grain of Body Centered Cubic (BCC) Iron crystal. Their study involved having an initial crack size (a_o) of 2.5 µm and a distance from the grain boundary to initial crack tip (l_{GB}) of 1.25 µm. To obtain possible crack paths, Hansson and Melin varied their crack angle (α) from 0 to 90°, with the presented results primarily being found with α equal to 35.3°, 45°, and 54.7°. Finally, the load cycles they used a maximum load ($\sigma_{yy\ max}^{\infty}$) of 200 MPa and a minimum load ($\sigma_{yy\ min}^{\infty}$) of 0 MPa. Overall, the model boundary

19

and plasticity were built from dislocation dipole elements and discrete dislocation, respectively. The result of the model was that the crack growth could be modelled from emission and annihilation of the discrete dislocations. The formulation of the model allowed Hansson and Melin to quantitively describe the zigzag pattern that crack growth tends to take and the development of the plastic zone around a crack tip. Fundamentally, Hansson and Melin found from their results that the grain orientation and activated slip system orientation were the primary factors that determined crack growth.

The reports covered in this section reinforced the importance that dislocation and microstructure size plays in the crack growth and fatigue life of a material. From Hansson and Melin [13], the ability to characterize crack growth through dislocations and slip systems implies that their formulation can be applied to other materials. From the papers by Zhang et al. [10] and Watanabe et al. [12], it can be surmised that regardless of material, microstructural characteristics define the effects of fatigue. Seeing how important dislocations are to crack growth and how microstructure plays a large role on fatigue on other materials is used as a guide in the present study.

2.3 Nickel-Based Superalloy Fatigue

This subsection will discuss literature that focuses on nickel-based superalloy fatigue. These reports provide an overview of what work has been done regarding the fatigue research done on superalloys. The benefit of this set of papers is that they more directly relate to the present study than the previous section. This section is separated into two subsections: Low Cycle Fatigue and Further Fatigue Effects.

2.3.1   Low Cycle Fatigue

This section discusses papers that particularly focus on how microstructure characteristics play a role in Ni-based superalloy fatigue while subjected to low cycle fatigue (LCF).

The first paper is by Larrouy et al. titled "Grain boundary-slip bands interactions: Impact on the fatigue crack initiation in a polycrystalline forged Ni-based superalloy" [15]. In their paper, Larrouy et al. study nickel-based superalloy with different microstructures to focus on the plasticity and damage processes developing near grain boundaries. Also, the slip transfers between neighboring grain boundaries based on local crystallographic orientations. The testing was conducted on two configurations of Udiment 720Li (U720Li) alloy at room temperature. The first configuration had bimodal grain size distribution with clusters of small grains merged on a coarse grain skeleton. The second configuration, made specific for the study, had a homogeneous coarse grain structure with fine intragranular γ' precipitate. The testing focused on the development of "micro-volumes" from the interaction of slip bands with grain boundaries. From their testing, Larrouy et al. found that regardless of the microstructure configuration, the formation of small volumes (characterized as ~30 μm3), along local crystallographic rotations, at the tip of the interacting slip bands and grain boundary. Based on the EBSD observation, the micro-volumes cause high local stresses in the structure. They further conclude that a twist angle greater than ~55° was needed for their development and the formation was favored at grain boundaries where slip transmission was difficult. Finally, it was observed that the micro-volumes were the origin of fatigue cracking.

Another paper focusing on LCF behaviors is by Kim et al. [16] titled "Effect of microstructural characteristics on the low cycle fatigue behaviors of cast Ni-based superalloys." This paper is another one with the goal to observe the effects that a material microstructure has on the LCF of superalloy. This focuses on the effects of low temperature vs high temperature testing and the role γ' plays in the microstructure. In their experimentation, Kim et al. work with two kinds of superalloys: Hastelloy X and Inconel 738LC. Their testing involved the use of an Instron 8501

testing machine and observation done by Optical Microscope (OM), SEM, and TEM. The fatigue testing was conducted at 0.25 Hz with a temperature range from 650-927 ℃ and a strain range from 0.6-1.2%. One of their first findings is that the fatigue life of the IN738LC is different based on the strain and temperature loading. Similar to what was found my De La Torre [2], the fatigue life of IN738LC at 650 ℃ with 0.4% strain was higher than at 927 ℃. However, the fatigue life was greater at 927 ℃ than at 650 ℃ when the strain was increased to 0.6%. In the case of Hastelloy X, fatigue life was always better at lower temperatures, regardless of strain increase. Kim et al. reiterate the well-studied trend that high ductility materials show better fatigue resistance in the plastic strain regime while high strength materials have better fatigue resistance in the elastic regime. Their fatigue testing supported this trend. The most important topic that Kim et al. address from their work is the negative effect that oxidation has on fatigue life. Based on their results, Kim et al. conclude that the reason why IN738LC has fatigue life at lower strains is because oxidation takes effect and increases the severity of crack initiation and its growth. However, they further conclude that the increase in strain and temperature leads to thermal activation of slip systems, allowing the strain to be more homogenously distributed. This finding supports the theory proposed by Mello et al.

Similar to the paper by Hansson et al. [13], Zhang et al.'s [17] paper "Grain size based low cycle fatigue prediction model for nickel-based superalloy" also discusses a way to model fatigue based on microstructure. They discuss how LCF life prediction models, such as the Coffin-Manson equation and the Ostergen energy method presented in his paper "A damage foundation hold time and frequency effects in elevated temperature low cycle fatigue" [18], are important tools for superalloys. However, Zhang et al. explain that the two models do not take into account the effect of material grain size, leading to the purpose of Zhang et al.'s study. Unlike Hansson et al. [13]

22

that did not work on a physical model, Zhang et al, worked with GH4698 superalloy and used an MTS 810 fatigue testing machine. The grain size based LCF fatigue life model that was found can be seen below in Equation 2.1, where $\Delta\varepsilon_t$ is the total strain amplitude, σ_{b0} is friction stress, k_b alloy related factor, P is a scale factor, E is elastic modulus, and m and n are material constants to be determined. After applying material parameters, Zhang et al. are left with Equation 2.2. In conclusion, Zhang et al. discuss how the new fatigue life prediction model is beneficial and has a high prediction accuracy based on their analysis. Finally, from the model, it is clear that fine-grain superalloys have a higher fatigue life than coarse-grain.

$$N_f = m\left[\Delta\varepsilon_t - \frac{P\left(\sigma_{b0}+k_b d^{-\frac{1}{2}}\right)}{E}\right]^{-n} \tag{2.1}$$

$$N_f = 2.49552x10^{-5}\left(\Delta\varepsilon - 3.6710x10^{-4}d^{-\frac{1}{2}} - 2.1567x10^{-3}\right)^{-2.93617} \tag{2.2}$$

The final paper for this subsection is by Salvat Cantó et al. [19] titled "A study of low cycle fatigue life and its correlation with microstructural parameters in IN713C nickel-based superalloy." As the name suggests, this paper also focuses on how microstructure affects LCF. Uniquely, they focus specifically on how three different kinds of microstructure within the material affect the fatigue life. The testing was done at room temperature and 650 °C with a strain of 0.2% to 0.6%. Salvat Cantó et al. conducted their observation following the fatigue testing using a Zeiss EVO LS25 SEM, EBSD, EDS, and an OM. The three forms of microstructures that was studied are the equiaxed, transition, and columnar structures with average grain sizes found to be about 5.88 mm^2, 7.83 mm^2, and 21.58 mm^2, respectively. The form of the three structures can be seen in the EBSD image in Figure 2.6. The finding from their fatigue testing is that the equiaxed grains had a fatigue life 10% better and 200% greater than the transition and columnar grains, respectively. This indicates that the grain size being smaller leads to a higher fatigue life as was

discussed by Kim et al. [16]. They discuss that the larger grain amount of grain boundaries causes a restriction in the crack propagation. Oppositely, the elongated grains of the columnar grains, especially in the direction of loading makes the crack propagation easier. As for the testing conducted at 650 ℃ the expected trend of fatigue life reducing across the board was observed. A final result was that cracking tended to occur on the surface of grains with a {100} orientation. Overall, this report had many of the same observations as the others in the subsection.
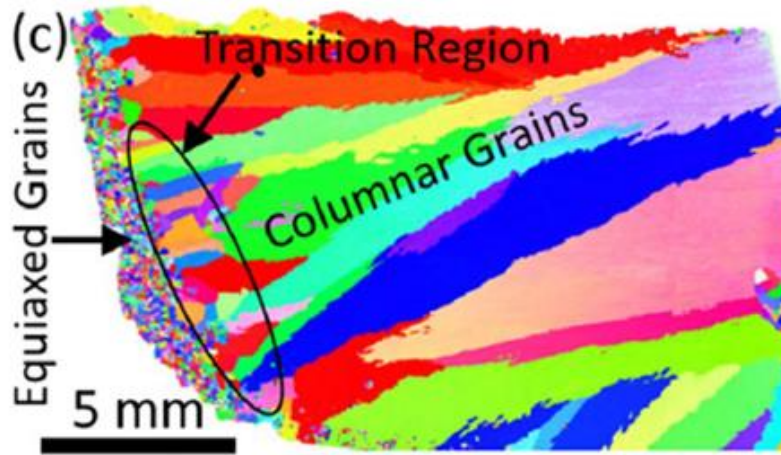

Figure 2.6: EBSD image of the equiaxed, transition, and columnar grains in IN713C. [19]

This subsection displays that in the case of low cycle fatigue, much research has been done to characterize what affects the fatigue life of nickel-based superalloys. It is clear that microstructural elements such as precipitates and grain size affect fatigue life but also the loading conditions such as temperature and strain.

2.3.2   Further Fatigue Effects

This subsection focuses on other fatigue characteristics that have been studied and on other cycles such as HCF and VHCF. Overall, this section discusses similar concepts from the previous subsection but more generally.

The first paper that will be discussed is "High temperature fatigue of nickel-based superalloy – A review with special emphasis on deformation modes and oxidation" by Pineau and Antolovich

[20]. This is an interesting paper as they cover LCF, HCF, crack propagation, and thermos-mechanical fatigue for Ni-based superalloys. Their purpose is to discuss these factors as they relate to deformation mechanisms, environmental effects, and the interaction between the two. As this report is a review of others, no experimentation was conducted. One of the conclusions made by Pineau and Antolovich is the interaction between oxidation and temperature. They discuss that at low temperatures oxidation is minimal, at intermediate temperatures the environment begins affecting damage, and finally at high temperatures the oxidation is greater, but deformation mechanisms make it irrelevant. This supports the findings the findings of Kim et al. [16] with the negative effect oxidation can pose to the Ni-based superalloys depending on material microstructure and temperature. But the trend found by Mello et al. [1] of the improved fatigue life by thermal slip activation improves fatigue life presented itself again in Pineau and Antolovich's [20] review. Another conclusion is that the severity of environmental effects is dependent on the interaction of microstructural and deformation. Generally, microstructures that have better stress relaxation have a better resistance to oxidation, which seems to be a common property of Ni-based superalloys. Overall, this review by Pineau and Antolovich summarizes many of the same topics that have been covered in the present literature review and well establishes the role of oxidation.

Next is the paper "Effect of Crystal Orientation on Fatigue Failure of Single Crystal Nickel Based Turbine Blade Superalloys" by Arakere and Swanson [21]. They discuss how nickel-based superalloys and their use in turbine blades and the occurrence of HCF failures, as discussed by Cowles [22], makes studying them important. Arakere and Swanson [21] studied the fatigue failure of PWA 1480/1493, a common single crystal Ni-based turbine superalloy by experimental LCF fatigue data and more interestingly, three-dimensional finite element modeling of turbine blades.

It is discussed that for single crystal materials, the position of the of the crystal lattice relative to the geometry plays a major role in fatigue effects. By studying 24 octahedral and 6 cubic clip systems for an FCC crystal and conducting 297 finite element models, the crystal orientation variation effects were found. Arakere and Swanson determined that the secondary crystal orientation (β) had the greatest effect on fatigue life. From their models, the failed turbine blades were found to have a β of about 50º. Arakere and Swanson conclude that controlling the direction of the crystal orientation can improve a nickel-based superalloy component's resistance to cracking and improve its fatigue life with minimal cost.

The research of single crystal superalloys is expanded by Cervellon et al. [23] in their paper "Crack initiation mechanisms during very high cycle fatigue of Ni-based single crystal superalloys at high temperatures." Unlike many of the previous papers, this study provides a unique perspective with its focus on VHCF ($>> 10^7$ cycles). Using a single crystal CMSX-4 Ni-based superalloy, their experimentation was done at 1000 °C, 20 kHz, and R = -1 and their observations were done with SEM, EBSD, and atom probe. Cervellon et al.'s most interesting result was an area they termed as the "rough zone" around a crack initiation site. Images of this rough zone are seen in Figure 2.7 below. They describe how this occurrence is similar to VHCF testing of high-strength steel at ambient temperature as discussed by Hong and Sun [24]. The formation of the rough zone was found to begin once 10^7 cycles are exceeded and the size of the zone increases as cycles to failure increases. Cervellon et al. further determined that the stress intensity factor of the area (K_{RZ}) was found to be 2.15 MPa*m$^{1/2}$ in mode-I and 1.25 in MPa*m$^{1/2}$ mixed-mode. In general, the rough zone was characterized by local regions of high dislocation density due to stress concentrations while the deformation is characterized by slip bands causing shearing of the γ/γ'

microstructure. While this case is conducted at VHCF, similar influences of fatigue within the rough zone are familiar.
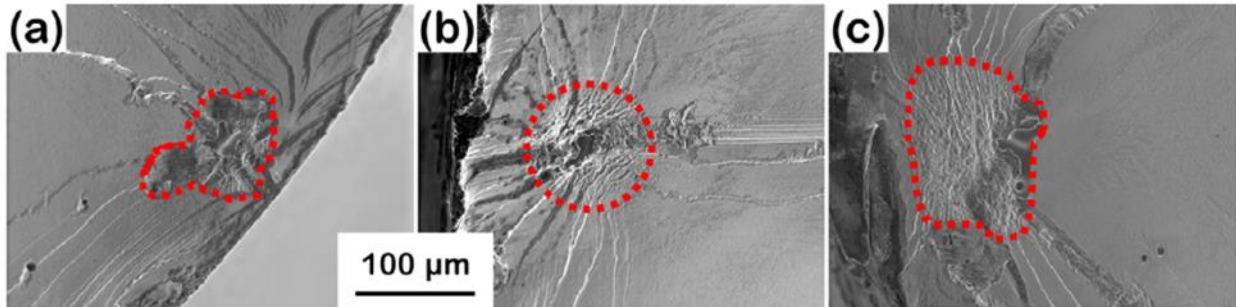

Figure 2.7: Rough zone on CMSX-4 Plus specimens tested at 1000 °C, 20 kHz, R= -1: (a) σ_a = 210 MPa, N_f = 7.58 x 10^6 cycles; (b) σ_a = 210 MPa. N_f= 4.66 x 10^7 cycles and (c) σ_a = 180 MPa, N_f= 1.72 x 10^8 cycles. [23]

Overall, this subsection reviews studies that either work beyond LCF or provide unique methods of studying fatigue along with LCF testing. However, these papers reinforce the role of microstructure and interactions with environment, loading, and temperature in fatigue life of Ni-based superalloys.

2.4 Related Concepts

This section discusses papers that cover other general topics that are related to fatigue, superalloy fatigue, and research methods that are used in the present study. As such, this section is separated into two subsections: EBSD Imaging and Fatigue Life Improvement. The EBSD Imaging subsection provides useful guidance for the EBSD imaging process that is conducted in this study. The Fatigue Life Improvement section covers papers that have studied methods of improving Ni-based superalloy and other material fatigue life.

2.4.1   EBSD Imaging

As the primary investigative work of this paper is dependent on the use of EBSD to characterize the microstructure of IN-718, similar work of EBSD analysis on nickel-based superalloy was studied. The first paper that provided background information on EBSD techniques was "Analysis

27

of activated slip systems in fatigued pickle polycrystals using EBSD-technique in the scanning electron microscope" by Blochwitz et al. [25]. They do not focus on Ni-based superalloys, however their study of slip systems for nickel polycrystals made this paper and worth reviewing. The main focus of this study was observing the trace angles of activated slip system and then comparing them to the expected trace to be able to determine the local stresses within the material grains. While the investigation of the nickel polycrystal is not strictly relevant to the present study, it is Blochwitz et al.'s use of EBSD to investigate slip systems that is relevant. Understanding the slip planes and slip bands in EBSD is important to be able to characterize fatigue in a material.

Expanding on imaging methods is the paper "Automated and quantitative analysis of plastic strain localization via multi-modal data recombination" by Charpagne et al. [26]. This paper presents a method of recombining multiple forms of data to be able to assess strain localization from the material microstructure. The combination consists of high-resolution digital image correlation (HR-DIC) data with crystallographic data from EBSD. This method was applied to Ti-6Al-4V and Inconel 718 and allowed thousands of slips bands and grains to be assessed. Charpagne et al. explain their process of using EBSD to determine material grain, then using HR-DIC to determine slip bands, and then overlapping the data. Figure 2.8 shows this overlap of EBSD and DIC data for IN-718. The result of their method is that the automatic detection of slip bands allowed for the identification of the slip system for over 90% of the slip bands. In the IN-718 testing, Charpagne et al. found that initial slip bands for parallel to twin boundaries, which are also the most intense slips, leading to high strain localization in relatively small grains. This paper is highly relevant to the current study as it provides important guidance for potential methods of data collection using SEM tools.
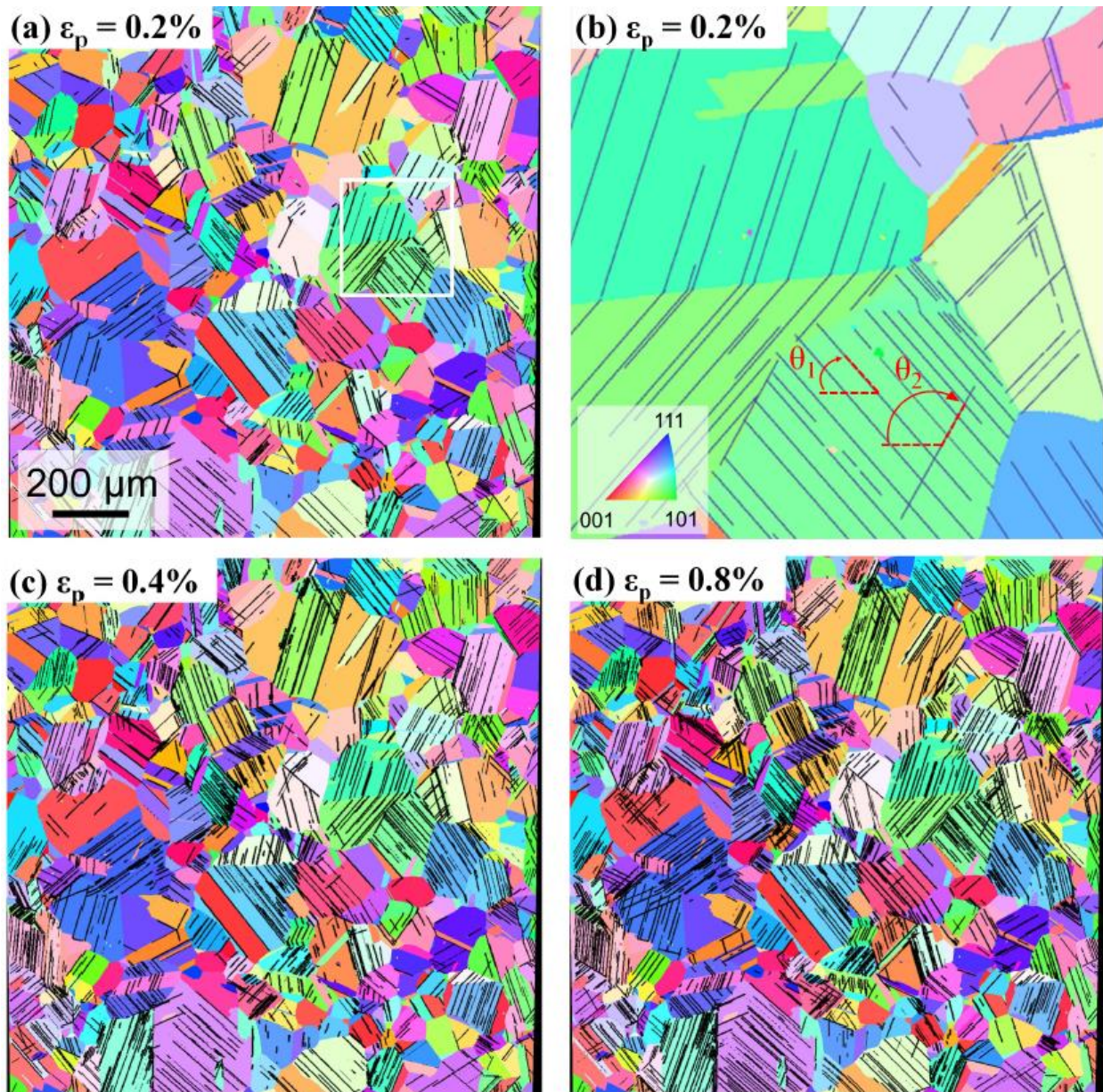
Figure 2.8: Overlap of the segmented slip bands and IPF colored EBSD map after merging, in the Inconel 718 material. a) $\epsilon = 0.8\%$, b) area framed in white on a), c) $\epsilon = 1.0\%$, d) $\epsilon = 1.4\%$. [26]

The main benefit of these two papers is their discussion and introduction of SEM/EBSD/DIC imaging and it can be used to well assess the stress and plasticity of a material. Essentially, studies being conducted using these imaging methods have validated the mathematical understanding of fatigue and material characteristics that affect fatigue life.

29

2.4.2   Fatigue Life Improvement

While fatigue in general is well studied and is being better understood for complex materials, much research is being conducted on how to improve fatigue life. The paper by Shao et al. [27] titled "Overview: Additive Manufacturing Enabled Accelerated Design of Ni-based Alloys for Improved Fatigue Life" provides a summary of what work has been done concerning at the role that Additive Manufacturing (AM) plays in improving fatigue life. Shao et al. explain that the application of AM to nickel-based superalloys is due to the complex components that the material is used for. The argument is that the machinability of this material is poor, making the complex structures difficult to manufacture. As such, the use of AM has the potential to make the manufacturing of the nickel-based superalloy components more efficient. In general, Shao et al. discuss the limitations of the study of AM for High-Cycle and Very-High-Cycle fatigue in nickel-based superalloys. Their overview consisted of discussing fatigue damage in FCC/FCC-like metals, loading frequency effects, composition/microstructure effects, and fatigue modelling for HCF and VHCF to provide background. From this, the discussion turned to present knowledge gaps, opportunities to improve HCF/VHCF performance, and conclude with future outlooks of AM research directions. In the outlook section, Shao et al. explain how it is known that the largest detriment to AM material performance is AM induced defects as described by Yadollahi and Shamsaei [28]. In particular, the existence of PSBs and their effects on fatigue requires surface treatment. They note that potential areas of research involving surface treatment include surface re-polishing, surface hard coatings, and heat treatment methods. Some key takeaways from Shao et al. are that the gaps of research involving how best to optimize the AM nickel-based alloy are how adjustments to the microstructure and composition affect dislocation behavior and how does cyclic frequency affect the dislocations. Based on the points presented by Shao et al. it is clear that addressing these gaps of knowledge and following potential AM research could lead to AM being

30

a great tool to optimize the fatigue life of nickel-based superalloys. As it has been established, the fundamental key to fatigue characterization is based on material microstructure and loading type and these continue to play a role in AM application.

A unique study was done by Aramesh et al. [29] and discussed in their paper "A novel treatment for cutting tools for reducing the chipping and improving tool life during machining of Inconel 718." As introduced in the previous paper by Shao et al. [27], the strength and resistivity of superalloys makes machining of components difficult. It has been documented that formation of cracking and chipping occurs on the machining tool itself. Overall, this paper does not expressly focus on fatigue of nickel-based superalloys themselves, but rather the wear and fatigue of the tools used on them. Aramesh et al. make it clear that the occurrence of chipping of the machining tool can yield damage to the surface of the superalloy, thus reducing its own fatigue life. This study discusses using a tool treatment method that controls chipping and improves the performance of the machining tool when working on Inconel 718. The proposed treatment method involves pre-machining the tool on an aluminum-silicon (Al-Si) workpiece before machining IN-718. Aramesh et al. worked on a Boehringer CNC turning center. Using a Tescan Vega II LSU SEM with an Oxford X-Max 80 Energy-Dispersive X-ray Spectroscopy (EDX) detector, they were able to study the effects of chipping and the application of pre-machining. The result of the pre-machining is that a thin layer of Al-Si would form on the tool surface. During the machining of the IN-718, the Al-Si would melt and then channel itself into the microcracks that would begin to form on the tool. The Al-Si layer would also lead to less friction and force necessary to be applied to the IN-718 machining. From their testing, Aramesh et al. found that the pre-machining led to a 300% improvement of tool life due to the reduction in chipping and crack formation. The forces required to cut the IN-718 was reduced by 40-50% on the treated tool. Another result is that the IN-718

specimen had an improved surface integrity, thus having an improved life. Again, while this study focused far more on the machining tool itself, it is important to note how the machining process of nickel-based superalloy can cause surface damage that reduces the fatigue life of the superalloy.

Finally, a paper the pertains well to the present study is "Improving the High-Cycle Fatigue lives of Fe-30Mn-0.9C Twinning-Induced Plasticity Steel through pre-straining" by Wang et al. [30]. Similar to the work conducted by De La Torre and Mello [2], Wang et al. compare the fatigue life of normal twinning-induced plasticity (TWIP) Fe-30Mn-0.9C steel and pre-strained TWIP steel. To conduct the testing and investigation, they used an Instron 5982 testing machine, a LEO SUPER 35 SEM, OLYMPUS 4000 Laser Scanning Confocal Microscope, and an FEI Tecnai F20 TEM. For their studies, six specimens were strained at 10, 20, 30, 40, 50, and 60 percent and then compared to unconditioned samples. The results of Wang et al.'s testing can be seen in Figure 2.9 below. They conclude that the pre-strained samples of the TWIP steel led to an improved yield strength and the formation of high-density deformation twins as seen in Figure 2.9(d). This resulted in the restraining of fatigue damage and thus yielding improved fatigue life.
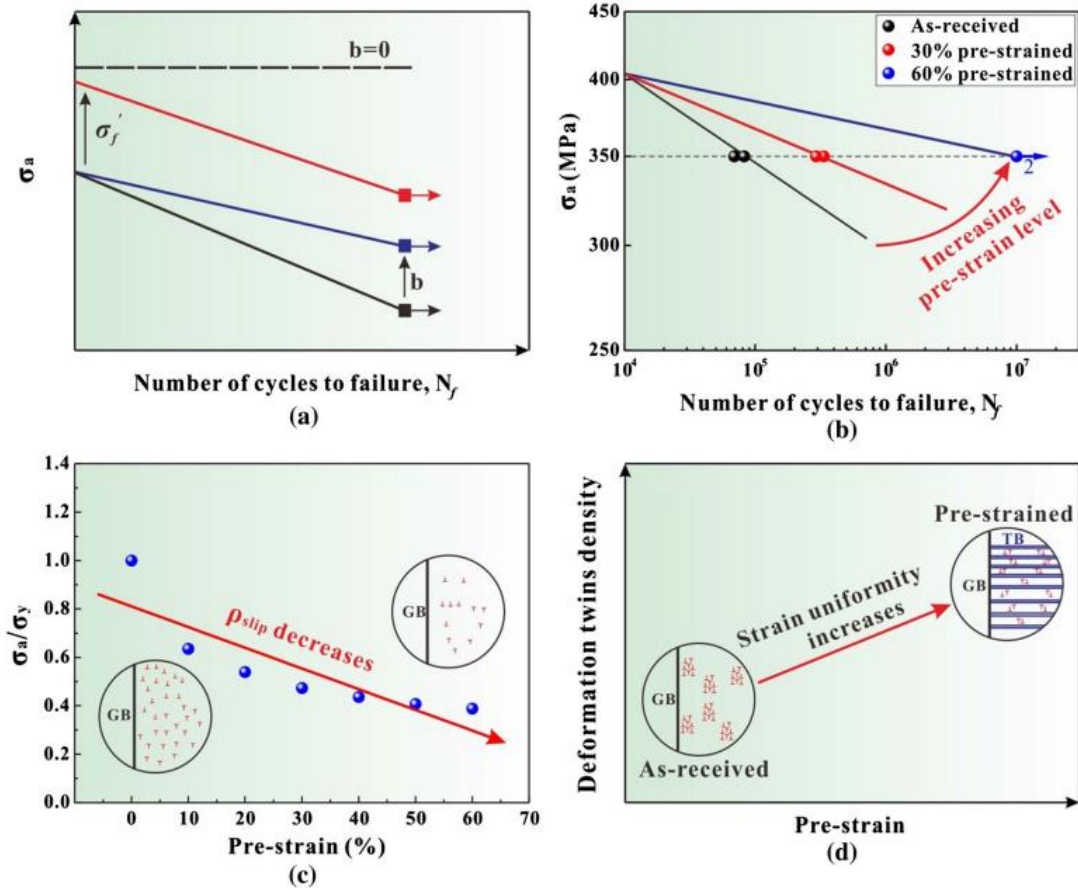
Figure 2.9: Schematic illustration of improvement for fatigue properties. (a) σ_a-N_f curves; (b) σ_a-N_f curves of pre-strained steel; (c) σ_a/σ_y ratio vs pre-strain curve of pre-strained steel, and the insert images showing the slip dislocation density under cyclic loading; (d) dislocation pile-up at grain boundary and twin boundary under cyclic loading. [30]

Overall, these papers introduce some research that is being conducted that relates to the improvement of the fatigue life of nickel-based superalloys. What is important to note is that this area of research is modern and is currently being explored. Another important note is that the improvement of a superalloy's fatigue can be applied to not only the material itself, but also the processes used to make the material. Finally, there is similar work being conducted on other materials and their findings can guide the research specific to nickel-based superalloys.

2.5 Summary

This review covers research that either focuses on nickel-based superalloy fatigue directly or similar topics that are related to the present research. The most important takeaway from this review is that the effects that material microstructure has in influencing fatigue has been well studied and primarily depends on particle size, grain size, and boundary density. Paired with different temperature levels and testing levels, the fatigue interactions within the material are complex. The findings of fatigue research involving other materials provide results that are comparable to the findings of Ni-based superalloy research. There is also research being conducted that covers methods of improving fatigue life. As such, the concepts covered in these papers are important to apply to the present research.

2.6 Hypothesis

Based on the reviewed research, the findings by Mello et al. [1] regarding the improved fatigue life at high temperature, high strain testing is supported. Given this and the resulting improved fatigue life found by De La Torre and Mello [2], it is the authors hypothesis that there is a shift in the material microstructure during preconditioning that allows for the strain to be better accommodated in both the octahedral slip plane {111} and the thermally activated cubic slip plane {100}.

3. Methodology

This section will outline the processes and materials used to conduct the research of nickel-based superalloy subjected to strain preconditioning to examine if resulting improved sample fatigue life has a microstructural cause.

3.1 Research Approach

This research has the main objective to show that thermal cube slip activation takes place on IN-718 when the conditions are applied as described by De La Torre and Mello [2]. As the purpose of this research is to investigate the potential cause of what De La Torre found, the methodology of this research closely followed the work done in her paper with regards to preparation. However, we will inspect the grains via SEM imaging and EBSD to prove or disprove the hypothesis adopted by the previous work.

3.2 Procedures

The procedure followed in this research is based on best practices of sample preparation with variation to fit the needs of this research. The apparatuses used to conduct this procedure are presented in the following section. The first stage for this work was preparing the Inconel 718 samples so they can be used for SEM and EBSD imaging. This stage is necessary to be able to conduct SEM and EBSD imaging on a sample consistently as the investigation is conducted. The first step in the preparation stage was polishing the two samples to ensure their surfaces would have as perfect a mirror-like finish as possible. The polishing of the samples was conducted by 600 Grit, 1200 Grit, and Nappad with Colloidal Silica solution until a mirror finish was achieved. To easily polish both samples at the same time, they were attached to an aluminum circular block using double-sided heavy-duty tape. Following the polishing, the next step was cleaning the samples to ensure no residue was present on the surface. This was done by placing the samples individually in vials filled with different cleaning chemicals and then sonicated for a certain time.

The order of the cleaning process was Acetone for 5 minutes, Isopropyl Alcohol (IPA) for 10 minutes, and Methanol for 5 minutes. Following the methanol cleaning, the samples are considered fully clean, and each is placed in separate vials marked accordingly. Figure 3.1 shows the samples on their aluminum block mount following polishing.
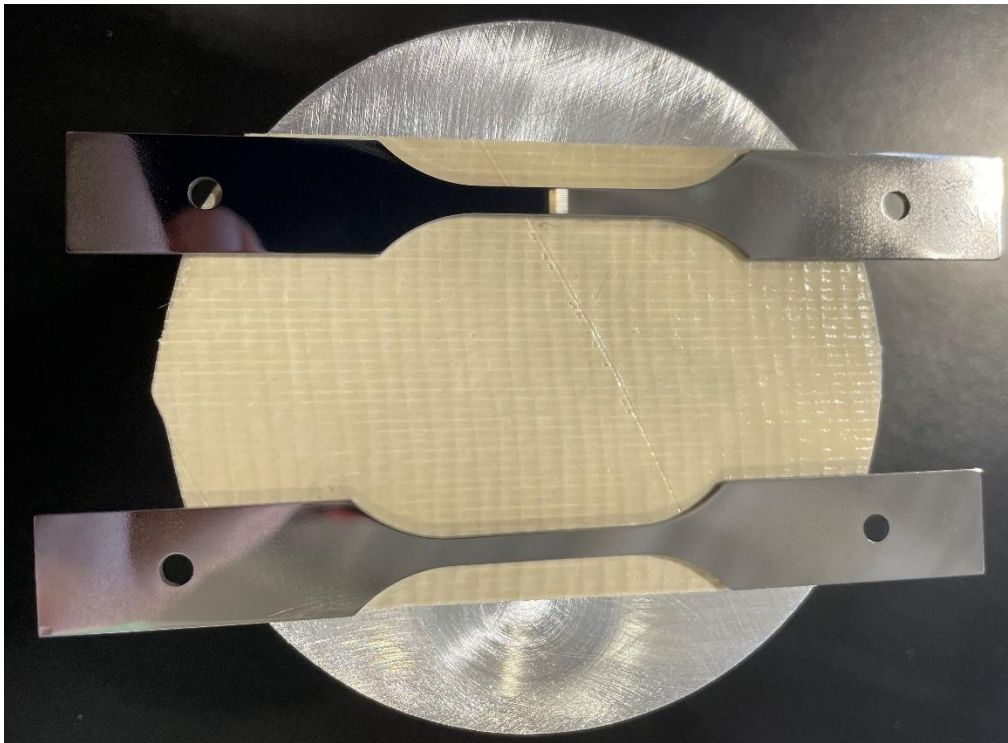

Figure 3.1: Polished samples on aluminum block.

Following the cleaning stage, the next step was marking the samples with designated study areas, or Areas of Interest (AOI). This step made use of the Wilson ® Tukon™ 1102 Micro-Indenter, able to apply loads from 10 to 2000 grams with a diamond shaped indenter. Figure 3.2 below shows a diagram of the positioning and the force used to make each marker. Indent 1 was the first indent made and was the reference point to create the remaining indents. This origin point indent was placed as close to the middle of the samples' neck area as possible, but this was mainly done by eye using the indenter's 50x magnification lens. The rectangle formed by the indents 2 through 5 denotes the area that will be studied using EBSD before and after preconditioning. The

purpose of indent 1 and the larger indent 6 are to use as markers to be able to find the study area when conducting SEM and EBSD imaging. Following the indentation of the samples, their positioning was confirmed using the SEM operating at 30 kV with a spot size of 4. Both samples were stored within the SEM chamber itself when not conducting EBSD so that oxidation of the surface would not occur and not impact the calibration of the EBSD imaging. This concluded the preparation of the research.
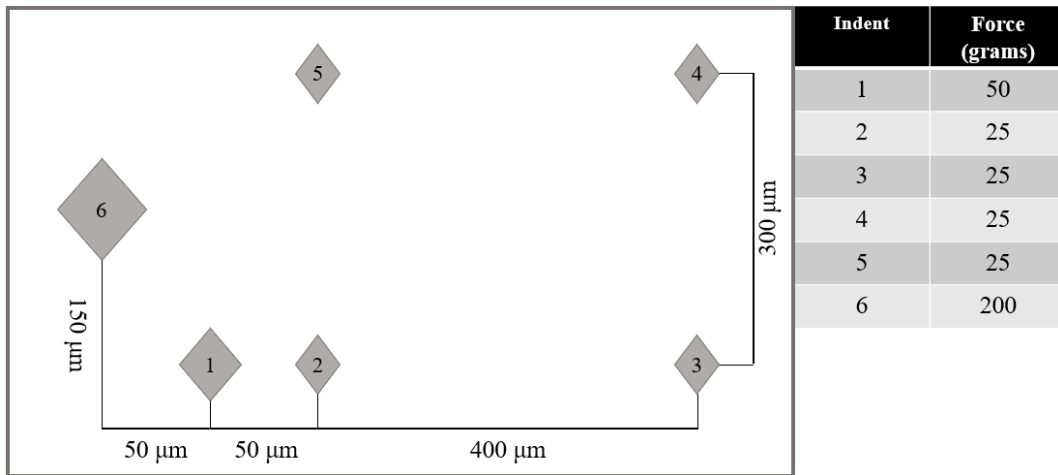

Indent	Force (grams)
1	50
2	25
3	25
4	25
5	25
6	200

Figure 3.2: Diagram of indentations and corresponding notation and force applied.

Following the sample preparation stage, the investigation stage is conducted. This stage involved the use of EBSD imaging and conducting sample preconditioning. For EBSD imaging, the sample apparatus was adjusted to be tilted at 70° within the SEM and the study area was found and focused on. The SEM was set at 20 kV and a spot size of 6. Using the ESPIRIT software, the EBSD is deployed and adjusted to image the study area. Following the initial EBSD imaging of both samples, both samples are preconditioned in the method that was done by De La Torre. For preconditioning, each sample was heated to 700 °C and then loaded along the sample x direction to a stress of 884 MPa with a 1-minute dwell time to obtain a corresponding 1.0% strain [2]. The samples' x-direction is defined along their length. Once the samples are unloaded and cooled, they are ready for the second EBSD imaging. The same process of sample preparation was followed

for the second round of imagining as was done for the first round. Once the second round of EBSD imagining was conducted, the experimentation phase was complete, and the imaging results are compared.

3.3 Apparatus/Materials

This section lists all the tools and materials used to conduct the sample preparation and investigation stages. The material being studied is the Inconel 718 nickel-based superalloy. The material properties of IN-718 can be seen in Table 3.1 [2]. Multiple samples were made from an IN-718 block using electro-discharge machining (EDM). The samples were machined to have a gauge length of 20 mm, a thickness of 1.25 mm, and a gage cross-sectional area of 3 mm. This dimensioning can be seen by Figure 3.3. The two samples were used in the present research. Each sample was previously marked with a separate number so the two samples are denoted as sample 1 (#15) and sample 2 (#4).

Table 3.1: IN-718 properties at room temperature. (AMS 5596M)

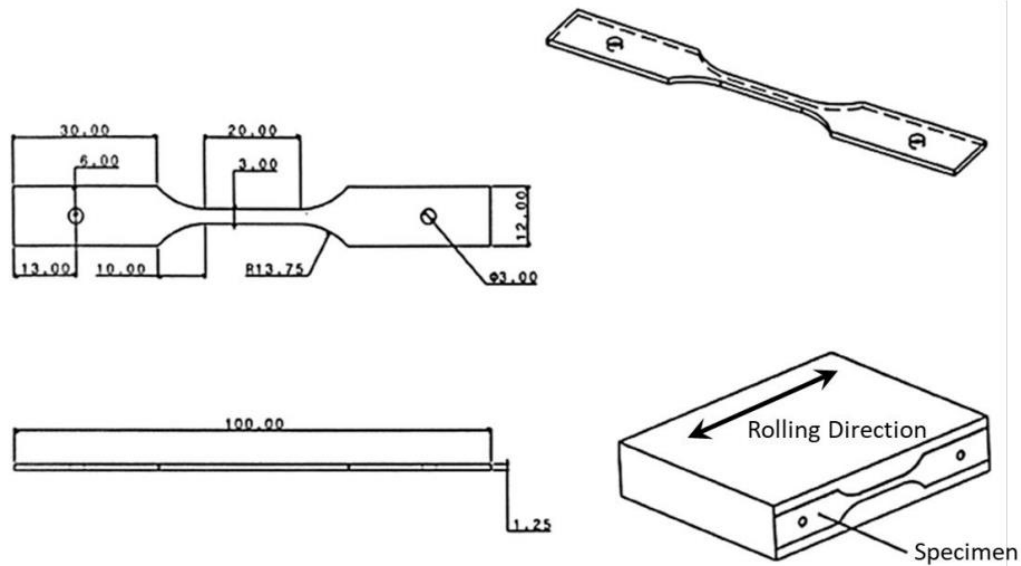| Properties	
Density, kg/m^3	8193.3
Melting Range,	1260 – 1336
Young's Modulus, GPa	199.9
Torsional Modulus, MPa	80 x 10^3
Poisson's Ratio	0.29
Tensile Strength, MPa	1241
Yield Strength (0.2% offset), MPa	1034
Elongation,%	12

Figure 3.3: Manufacturing drawing of the dog-bone shaped sample made of IN-718. All dimensions in mm. [2]

For the cleaning and preparation stages of the two samples, many different tools were used to reach the desired mirror finish on the samples' surface. Images of all the following can be found in Appendix A. The initial polishing was conducted using the Buehler Metaserv 250 Semiautomatic Twin Polisher (Figure A.1) followed by a 24-hour final polish in the Pace Technologies GIGA-1200 Vibratory Polisher (Figure A.2) with Pace Technologies Blue Colloidal Silica (Figure A.3). Following the polishing, the samples were cleaned and sonicated in a Branson Ultrasonic Cleaner (Figure A.4). To create surface indents to delimitate the study area, a Wilson Tukon 1202 Micro-Hardness Tester (Figure A.5) was used.

For preconditioning the samples, the main device used was the MTS Model 204.61 Servo Hydraulic System. Along with that, an MTS controller, ATS Series 3430 Split Furnace, and an ATS P-20-115 Temperature Controller. The samples were clamped using M-246 Clevis Couplings with a 273 mm pull rod extensors to ensure the specimens stay in place within the MTS frame and the ATS furnace (Figure A.6).

Finally, for the SEM, many different devices are set up. The key tools are the Bruker QUANTAX EDS for SEM and the Bruker QUANTAX EBSD sensors. These two can be seen in Figure 3.4, showing the overall setup of the devices. To conduct the SEM/EBSD imaging, the samples were mounted with the Carbon Tape onto sample holders. For the standard SEM imaging to verify the indentations, a flat holder was used. For EBSD imaging, the samples were attached to aluminum 45° holders. Once the samples were in the SEM, the stage was tilted an extra 25° to total the necessary 70° needed for EBSD imaging. In both cases, copper tape was used to ground the samples with the holder. Figure 3.5 shows one of the samples mounted to the holders EBSD imaging respectively.
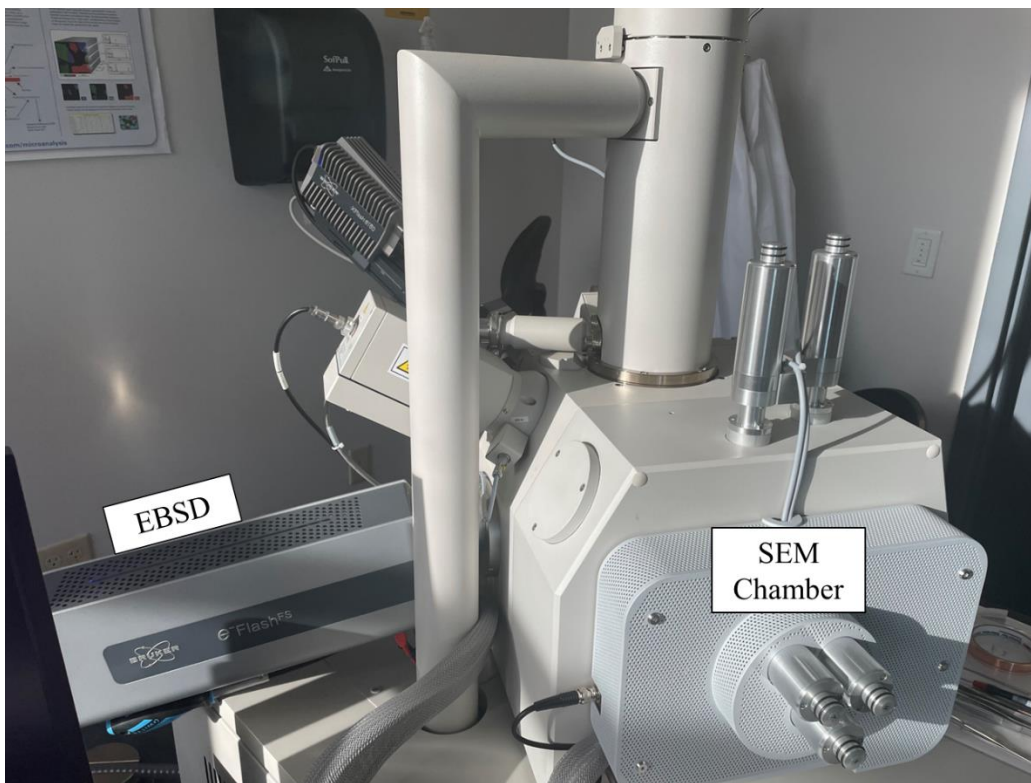
Figure 3.4: Bruker SEM and EBSD.

Figure 3.5: IN-718 sample mounted on 45° Aluminum holder with carbon and copper tape.

4. Results

This section will present the resulting changes from preconditioning and the images that were obtained using SEM and EBSD imaging of In-718 Samples 15 and 4. As such, the section is divided into the following four subsections: Preconditioning, Before Preconditioning, After Preconditioning, and Grain Comparison. The meaning behind the images will be discussed in Section 5.

4.1 Preconditioning

This subsection shows the resulting physical change to the Inconel samples following their preconditioning. As mentioned in the methodology section, the MTS testing machine and furnace were the key tools used to conduct the preconditioning. The specific dimensions of Samples 1 and 2 were measured to have gage lengths of 20 mm and 20 mm, gage widths of 2.91 mm and 2.92 mm, and gage thickness 1.19 mm and 1.22 mm, respectively. Using these specific dimensions, hand calculations were done to applied stress of 884 MPa for preconditioning to determine the specific input load needed to achieve 1.0% strain for each sample. The resulting loads are 3061 N (688.186 lb$_f$) for Sample 1 and 3149 N (707.860 lb$_f$) for Sample 2. The calculations can be found in Figure A.7. To account for potential reliability issues with the MTS load cell, 95% of the calculated load was inputted.

In the case of preconditioning sample 1, the testing was considered unsuccessful. While 700 °C was achieved, when slowly ramping up the MTS load input to a force of 2980 N (670 lb$_f$), the specimen fractured at about 2268 N (510 lb$_f$). However, this was not a total loss as the post-preconditioning SEM imaging was conducted as will be discussed later. The final dimensions of Sample 1 following the fracture were a gage width of 2.51 mm and a gage thickness of 1.08 mm. The gage length was not measured as the sample was now in two pieces. The result of specimen 1 can be seen in Figure 4.1.

Figure 4.1: Fractured IN 718 Sample 1 next to Sample 2. Axis included for sample direction.

With the knowledge that came from the fracture of specimen 1, better care was taken to conduct the preconditioning of sample 2. It was clear that basing the load control off the applied stress was not reliable due to the MTS machine's load control seemingly being unreliable. As such, the load was applied with a pre-check of the strain to achieve the desired condition. Once again, the temperature of 700 °C was reached in a very slow process to avoid overshooting. As the load was applied, the mechanism was closely watched to find the point where the specimen started experiencing permanent elongation. At that point, the load was sustained for one minute, as done

by De La Torre, to give time for the microstructure to settle. The resulting elongation can be seen in Figure 4.2. The final dimensions for specimen 2 were a gage width of 2.82 mm, and gage thickness of 1.21 mm.
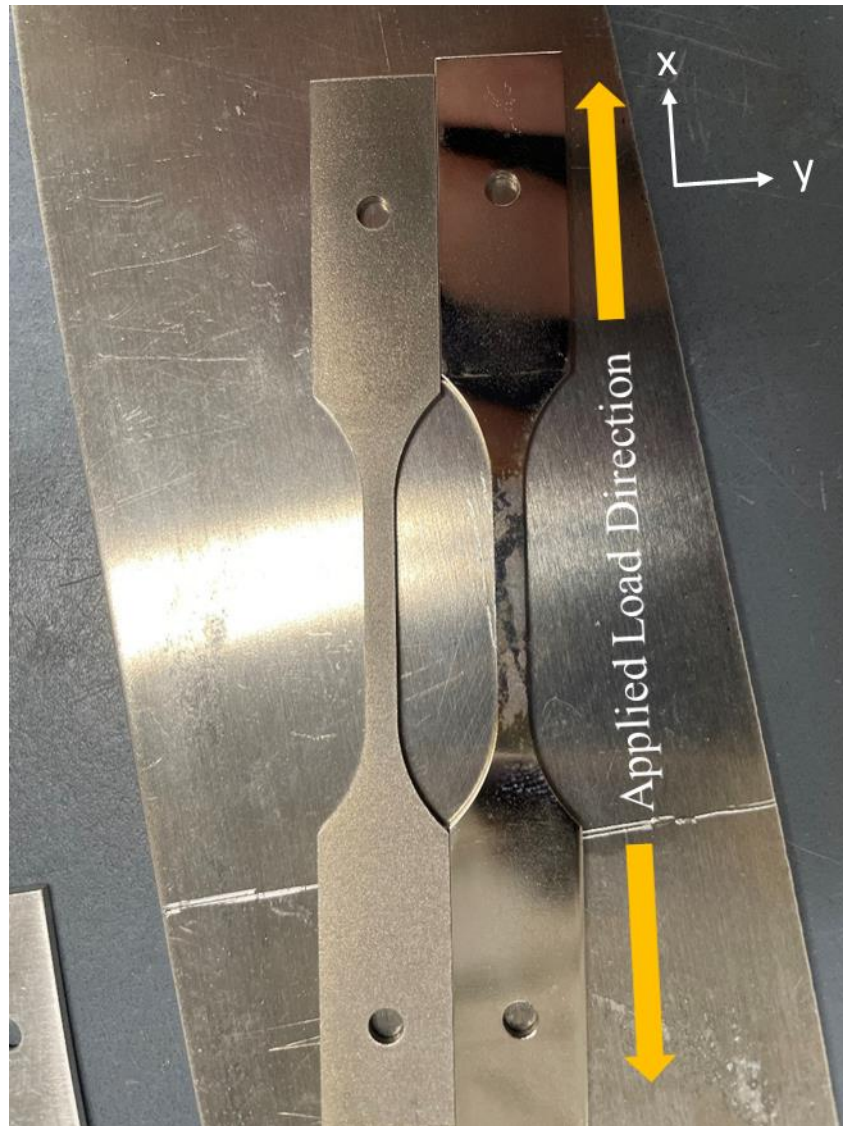
Figure 4.2: Elongated Sample 2 following preconditioning compared to standard IN 718 Sample.

Following the preconditioning, the second phase of the investigation using the SEM was conducted. However, before the results of that phase are discussed, the results of the initial investigation will be presented.

4.2 Before Preconditioning

This subsection presents the images generated for Samples 1 and 2 using SEM and EBSD. The

first set of images in Figure 4.3 are of the samples' AOI at the position needed for EBSD imaging.

The SEM voltage, magnification, spot size, and working distance can be seen at the bottom of each

image.
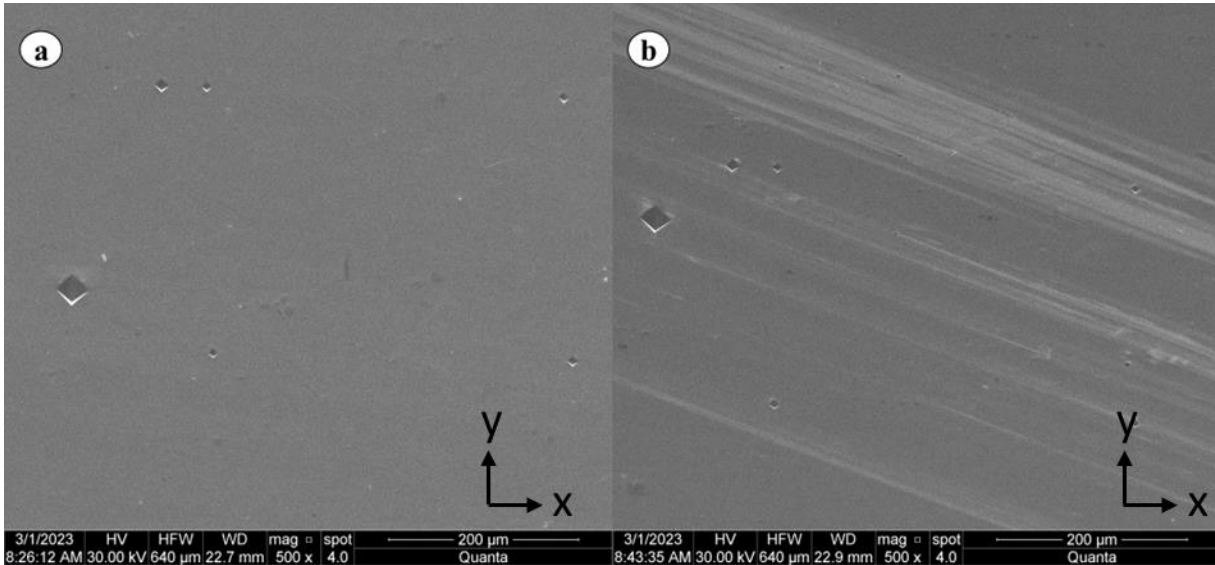
Figure 4.3: SEM image of AOI of a) Sample 1 and b) Sample 2. Sample axis included.

The following images consist of what was found using the EBSD. Figure 4.4 displays the grain

map of the AOI of Sample 1. Figure 4.5 displays the same map but for Sample 2. From the EBSD,

the specific crystal orientation was found for the most predominant grains in the AOI. The IPF-z

images of the samples along with a legend for the crystal orientations and the IPF map can be seen
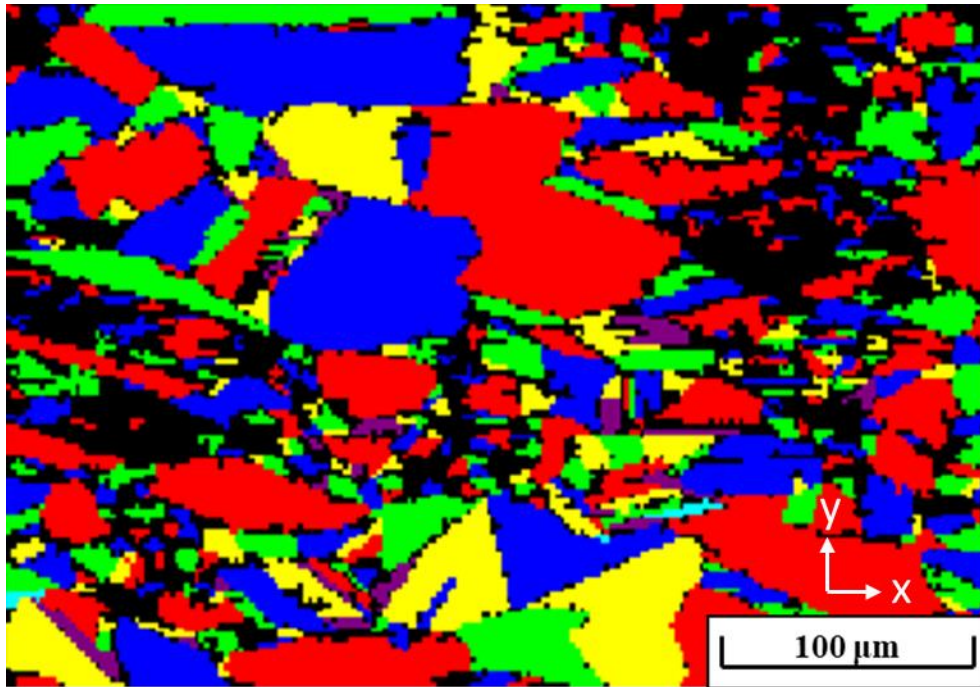
in Figures 4.6 and 4.7.

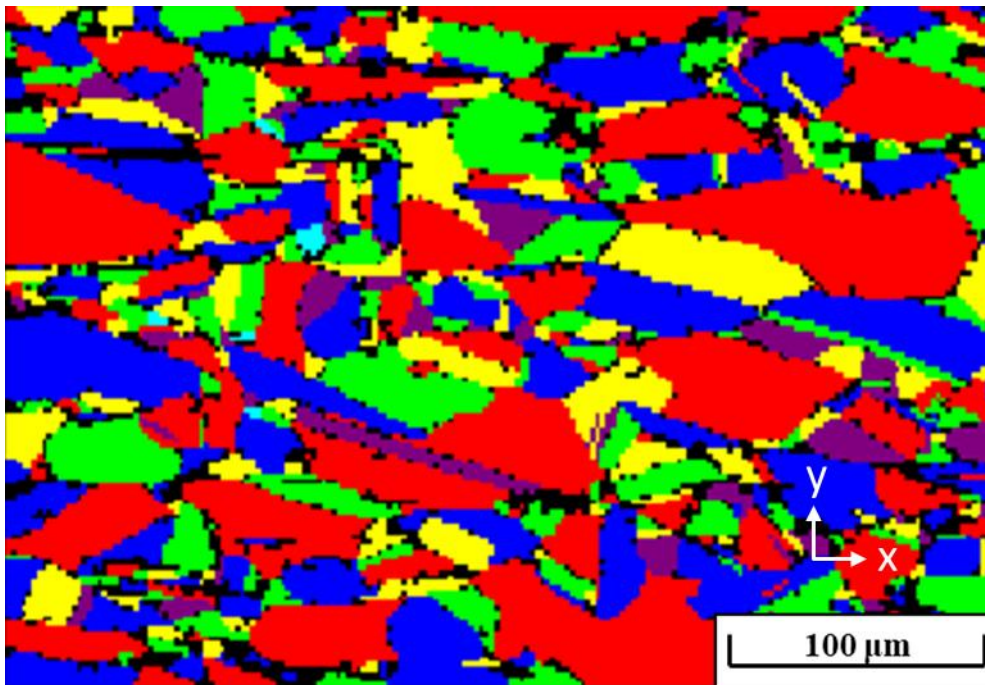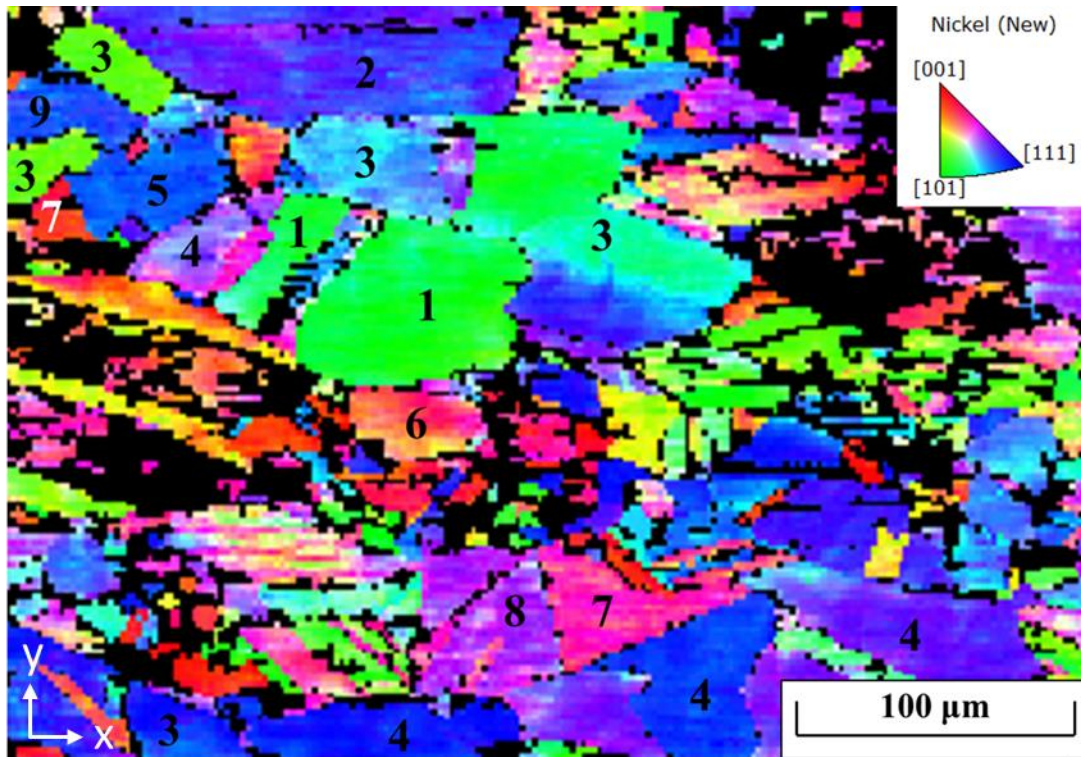*Figure 4.4:* AOI Grain Map of Sample 1.

Figure 4.5: AOI Grain Map of Sample 2.

Figure 4.6: Sample 1 IPFz map with numbered grains, crystal orientation legend and IPF guide map.
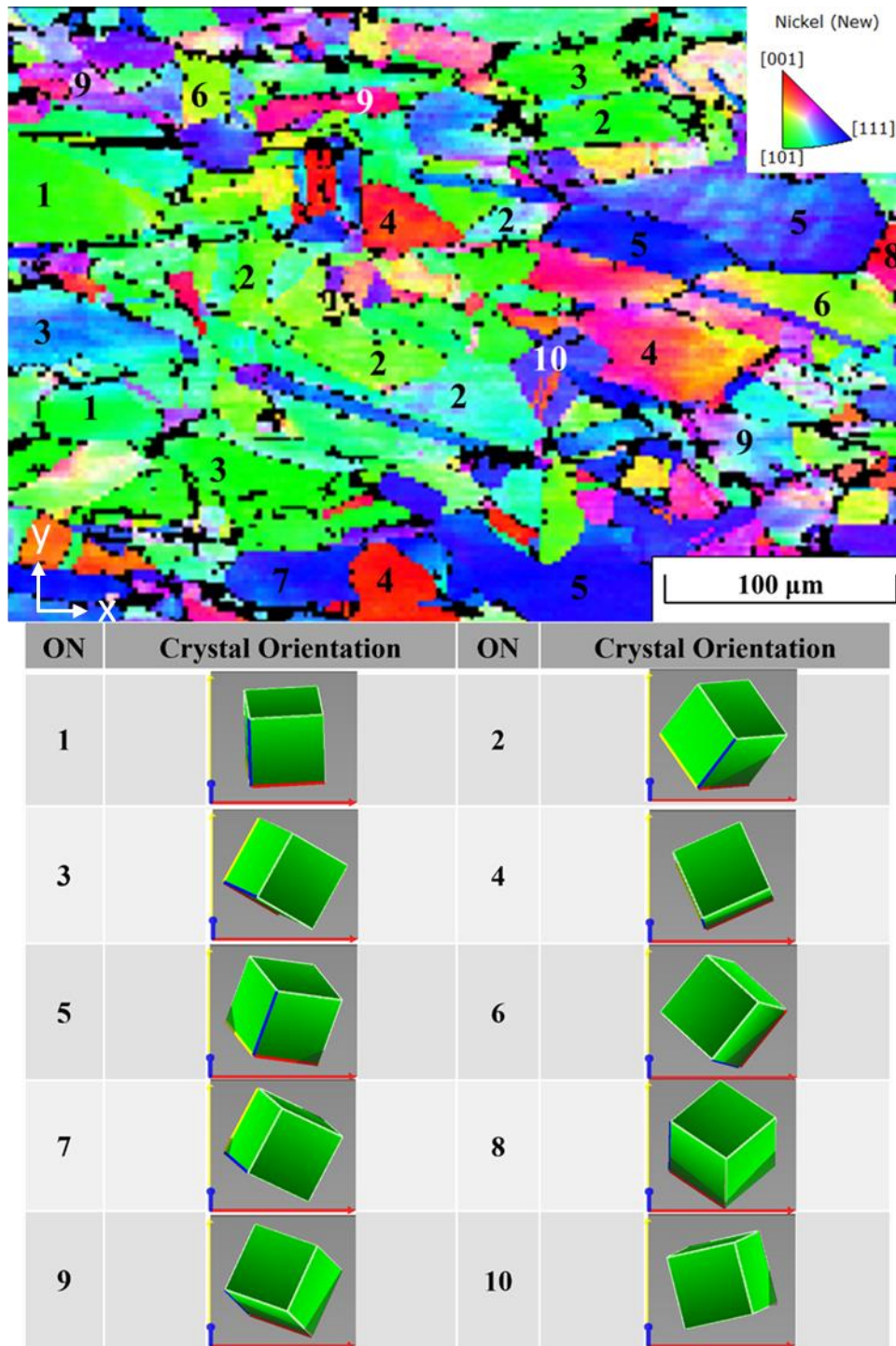
Figure 4.7: Sample 2 a) crystal orientation legend, b) IPFz map with numbered grains, and c) IPF guide map.

Using the IPF map, the grain boundaries were isolated and retraced. The trace was then overlayed onto the SEM images from Figure 4.3. Figures 4.8 and 4.9 present the following image

for each sample. By knowing the initial grain orientation and seeing the grain boundary applied to the SEM image, the initial data for the specimens is ready for comparison.
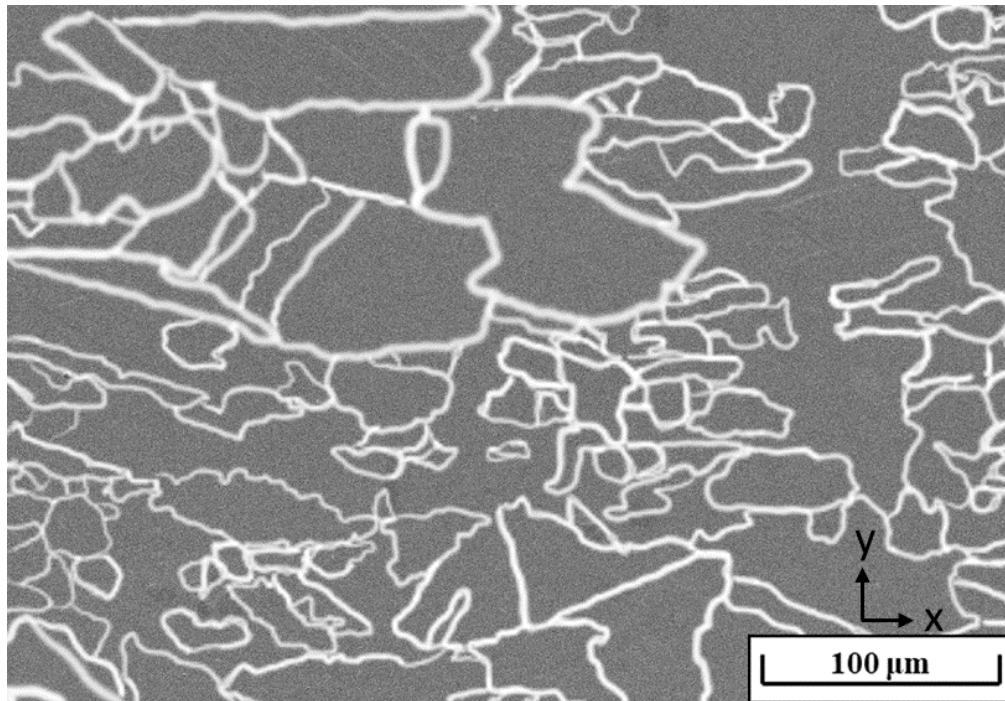

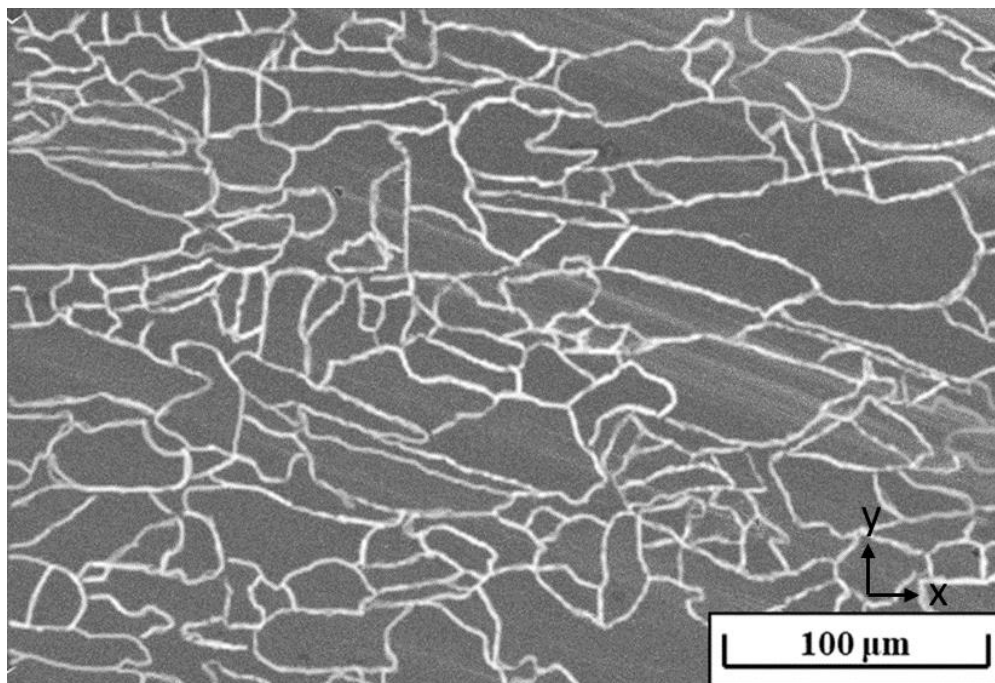*Figure 4.8:* Overlayed grain boundary on SEM image for IN 718 Sample 1.

Figure 4.9: Overlayed grain boundary on SEM image for IN 718 Sample 2.

4.3 After Preconditioning

Finally, the SEM images found following precondition are presented. EBSD imaging was not conducted following this step as the surface of the samples had been burned from the high temperature and would most likely produce poor images. The images of the AOI for both samples were found and can be seen in Figure 4.10 for Samples 1 and 2, respectively. Similar to what was done in the previous subsection, the grain boundary was retraced to make clearer for comparison. Figures 4.11 and 4.12 show the same images from Figure 4.10 along with the retraced grain boundary and highlights of the distinct slip bands visible in the grains.
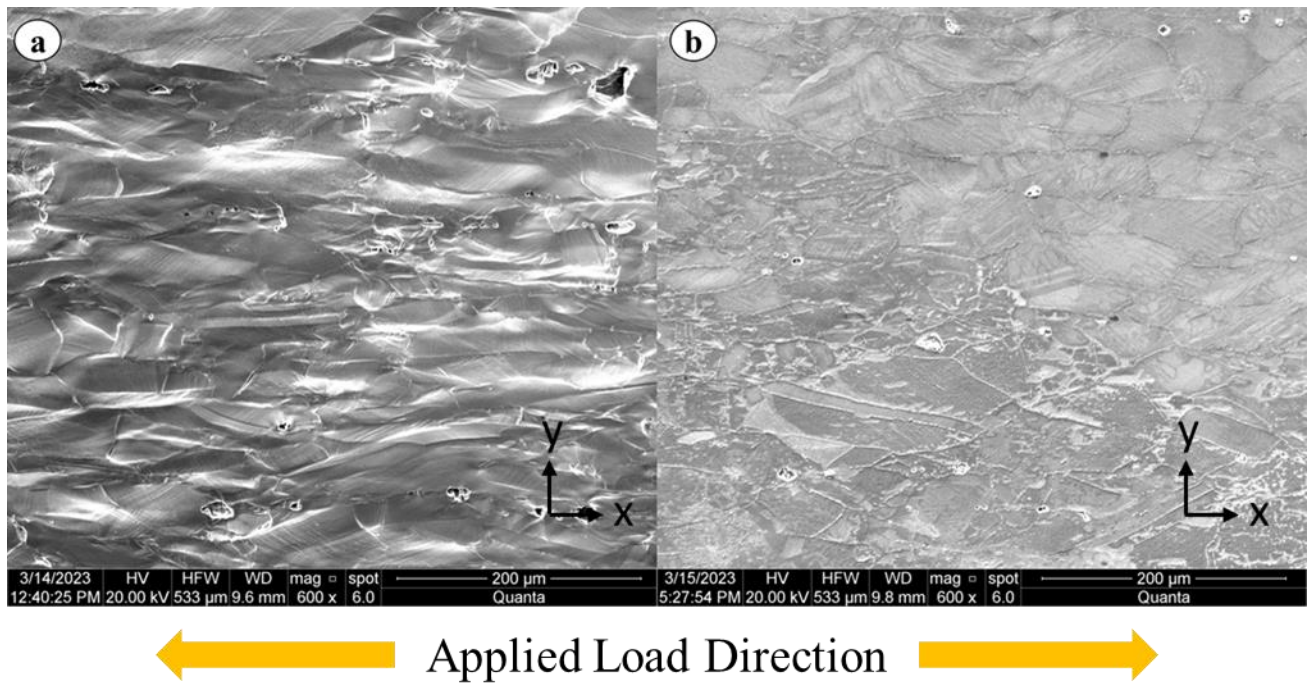

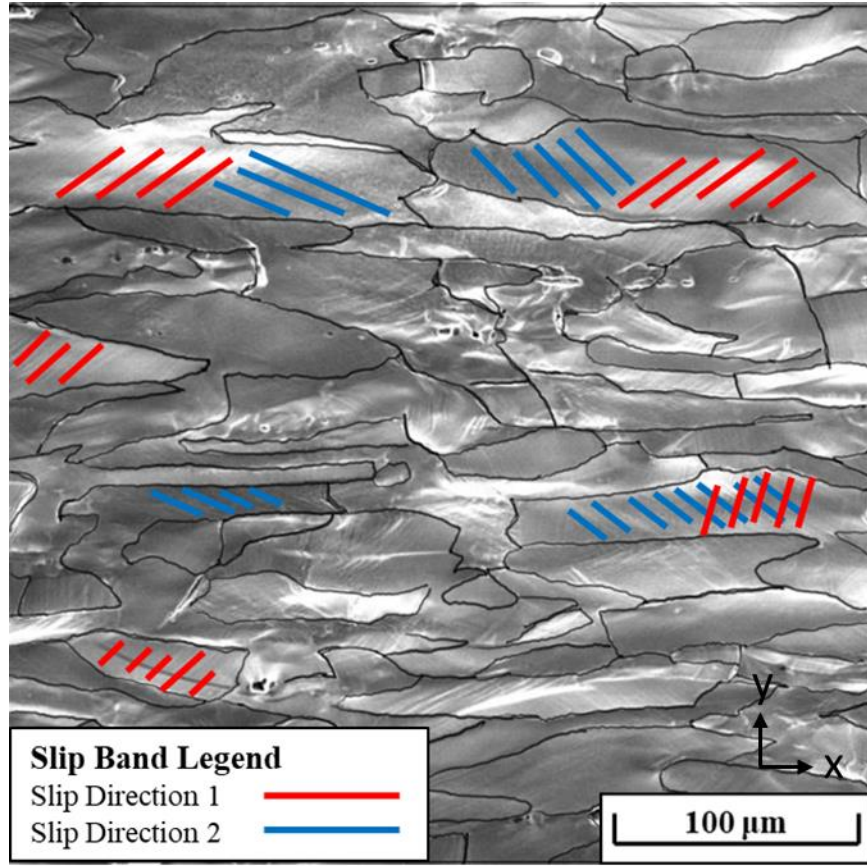*Figure 4.10:* SEM images following preconditioning for a) Sample 1 and b) Sample 2.

Figure 4.11: AOI for Sample 1, post preconditioning, with highlighted grain boundaries and slip bands.
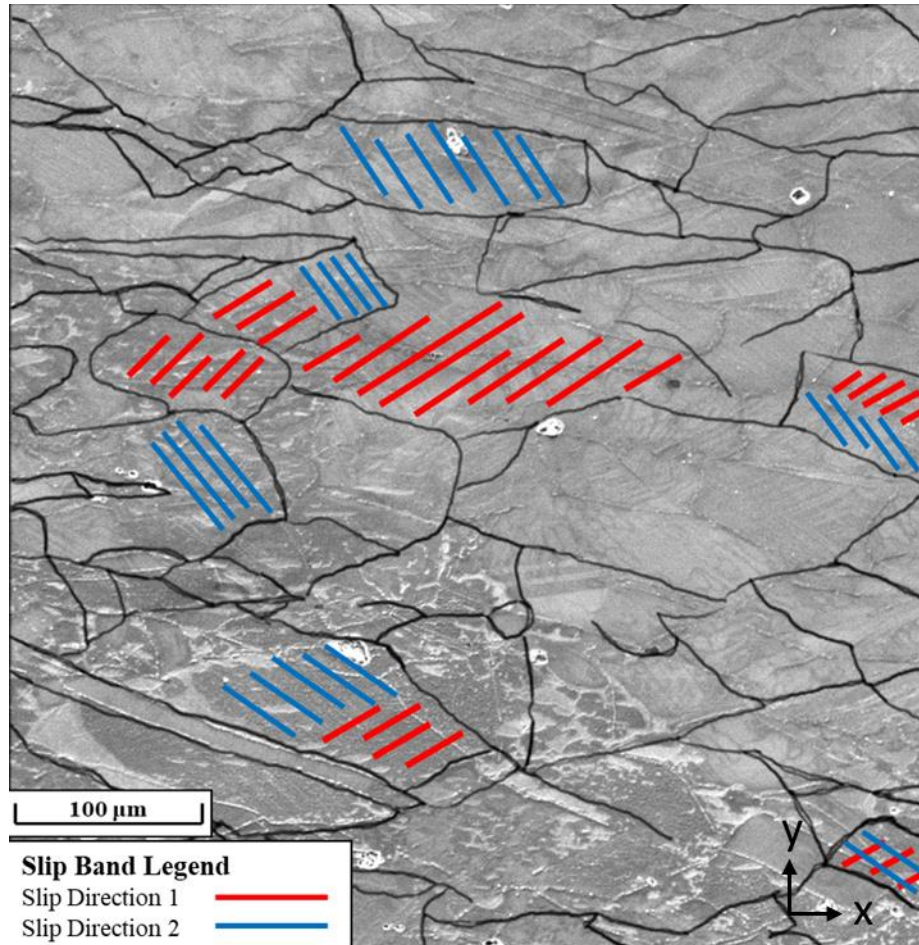
Figure 4.12: AOI for Sample 2, post preconditioning, with highlighted grain boundaries and slip bands.

4.4 Grain Comparison

With all the images found from the use of SEM and EBSD, the AOI grains, slip bands, and initial crystal orientation are compared. The first step was to examine the EBSD IPFz images found for Samples 1 and 2 (Figures 4.6 and 4.7) and then to find the equivalent grains in elongated preconditioned microstructure (Figure 4.10). Due to Sample 1 fracturing, the elongation of the grains within the AOI was so severe that it was impossible to clearly relate the grains from before and after preconditioning. As such, the grain comparison will be conducted on Sample 2. Figure 4.13 compares the initial EBSD image to the current microstructure and points out distinct grains between the two images.
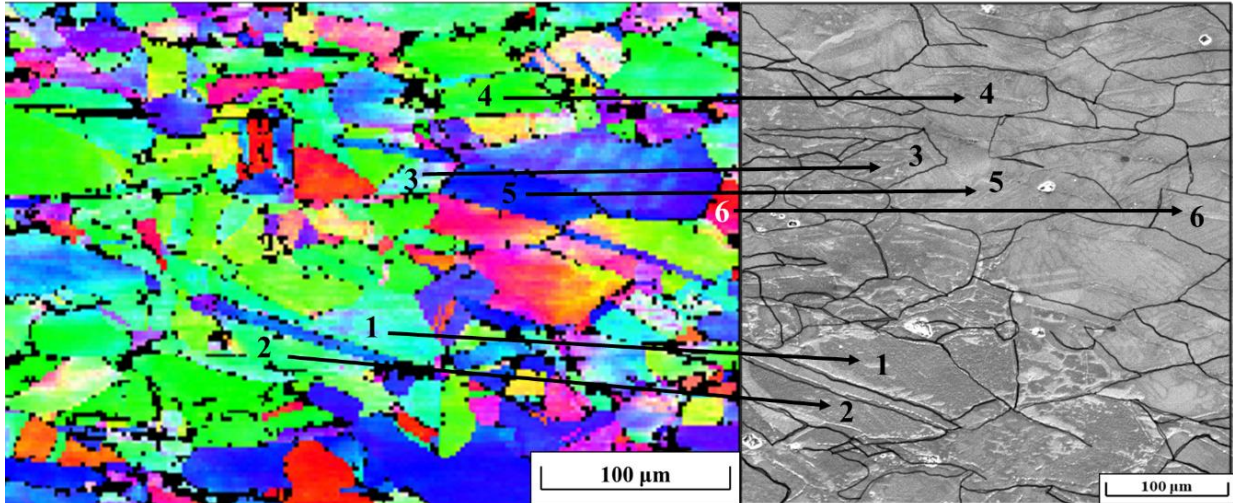
Figure 4.13: Displaying equivalency between Sample 2 grains before and after preconditioning.

As seen in Figure 4.13, there are six distinct grains that are pointed out. Grains 1, 3, and 6 clearly have two distinct slip band directions as can be seen in Figure 4.12. Grains 4 and 5 each have one of the respective slip band directions. These grains are individually compared to the original crystal orientation found from EBSD to determine if the projected slip bands are {111} or {100}. Figure 4.14 shows the specified grains in the AOI, their slip bands colored to match the direction along the crystal orientation (CO), and a graphic to represent the slip directions.
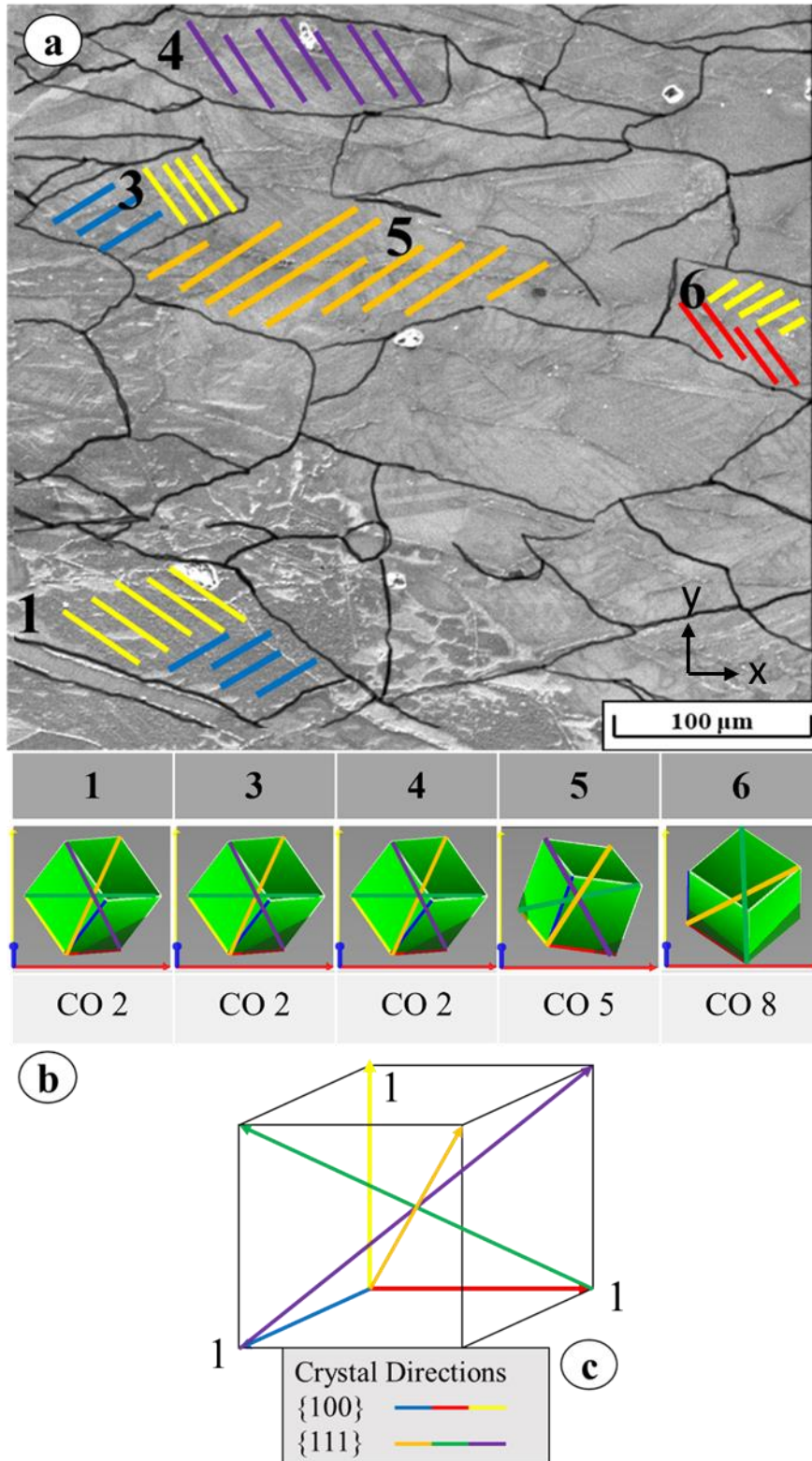
Figure 4.14: a) grains with characterized slip band directions, b) crystal orientation legend for each grain, and c) characterization of {100} and {111} directions in crystal for sample 2.

5. Discussions, Conclusions, and Recommendations

This final section provides discussions, conclusions, and potential recommendations based on the work conducted in this study. The answer to the question posed at the beginning of the paper is presented here.

5.1 Discussion

The first discussion point is the fracturing of Sample 1. The hypothesis as to why the preconditioning was a failure is that the load cell of the MTS machine was not properly calibrated. As such, the specimen fractured well before the calculated load that would result in 1.0% strain. When imagining the AOI of the sample, the significant elongation of the grains meant that finding the original grains was impossible so the final slip band directions. However, it can be observed that in Figure 4.10, nearly all the slip bands within the grains are bidirectional. The implication is that as the high temperature is sustained and the strain continuously increased, the microstructure was readjusting to the plastic loading. While the slip planes that are activated cannot be validated, this does at least show that a change has occurred.

This brings the discussion to the results of preconditioning for Sample 2. This sample was closely monitored during loading to avoid any negative effect on the results. The grains of the sample before preconditioning were found and characterized by their initial crystal orientation. After successfully drawing an equivalency between the grains before and after the preconditioning, the slip system of the grains was determined. Upon closer look at Figure 4.14, grains 4 and 5 displayed only one slip band direction. Comparing them to their respective crystal orientation (Orientation 2 and 5), it is clear that the slip bands are in the {111} directions. This shows that there was no change in those particular grains as the {111} direction is the default direction of the microstructure. In the case of Grains 1, 3, and 6, bidirectional slip bands were visible, similar to what was observed from the elongated grains of Sample 1. Comparing these grains to their initial

crystal orientation (Orientations 2, 2, and 8), the slip bands were found to reside in the {100} slip system.

5.2 Conclusions

The existence of grains with slip bands in both {111} and {100} slip systems, indicates that the cubic slip system was indeed activated by the high temperature and applied strain during the preconditioning. This seemingly supports that the increase in fatigue life in the IN-718 found by De La Torre and Mello can be caused by multiple slip plane activation causing microstructure homogenization, as with the activation of the cubic slip system alongside the octahedral system, the microstructure changed in a favorable direction, so the stress is better accommodated. This means that the strain localization is greatly reduced because of the preconditioning. Overall, this result supports the findings of Mello et al. [1] and other similar findings of the role that temperature and strain play in affecting fatigue life. The application of preconditioning on IN-718 does lead to improved fatigue life, and the activation slip systems may be the cause of this improvement.

5.3 Recommendations

Based on the work conducted in this study, two recommendations arise. First, is the potential to reproduce this test with the goal of improving the precision of preconditioning and potentially applying DIC to the material microstructure. The fracturing of Sample 1 means that improving load application could produce better results. This way, the results of the present study can be confirmed and further study on the material microstructural changes can improve the understanding of preconditioning a material. Secondly, in-situ experiments can be performed to follow the activation as load is applied. This type of research will need a special test frame and heater to operate inside a SEM chamber. This equipment is not currently available, but it is in the process of procurement within the Structures and Materials group at ERAU AE. Finally, with preconditioning seemingly confirmed to improve fatigue life, there is potential to study the

56

application of this method in the manufacturing of nickel-based superalloys. The only potential issue with applying this method is the fact that it works off plastic deformation of components. However, if this method can be applied, then components made of nickel-based superalloys with improved fatigue life can be manufactured and integrated as long as they are properly tested.

REFERENCES

[1] Mello, A. W., Nichols, A., and Sangid, M., "Fatigue strain mapping via digital image correlation for Ni-based superalloys: The role of thermal activation on cube slip," *Materials Science & Engineering A*, 2017, pp. 332-341.

[2] De La Torre, P. and Mello, A. W., "The effect of pre-thermal and -load conditions on IN-718 high temperature fatigue life," *Journal of Aerospace Technology and Management*, Vol. 12, No. 3, 2022, pp. 406-419.

[3] Dowling, N. E., "Mechanical Behavior of Materials: Engineering Methods dor Deformation, Fracture, and Fatigue," *Pearson*, 2nd edition, 1998.

[4] Sims, C. T., "A History of Superalloy Metallurgy for Superalloy Metallurgists," *Superalloys*, 1984, pp. 399-419.

[5] Smith, T., Duchao, L., Hanlon, T., Wessman, A., Wang, Y., Mills, M. and Mills, M., "Determination of Orientation and Alloying Effects on Creep Response and Deformation Mechanisms in Single Crystals of Ni-Base Disk Superalloys," *Superalloys*, 2016.

[6] Donachie, M. J. and Donachie S. J., "Superalloys: A Technical Guide," *ASM International*, 2nd edition, January 2002.

[7] Antolovich, S. D., "Microstructural Aspects of Fatigue in Ni-base Superalloys," *The Royal Society Publishing*, 2015, pp. 1-36.

[8] Walley, J. L., "Exploration of Local Strain Accumulation in Nickle-based Superalloys," *Ohio State University: Graduate Program in Materials Science and Engineering*, 2013.

[9] Pollock, T. M., and Tin, S., "Nickel-Based Superalloys for Advanced Turbine Engines: Chemistry, Microstructure, and Properties," *Journal of Propulsion and Power*, Vol. 22, No. 2, 2006, pp. 361-374.

[10]   Zhang, Z. J., An, X. H., Zhang, P., Yang, M. X., Yang, G., Wu, S. D., Zhang, Z. F., "Effects of dislocation slip mode on high-cycle fatigue behaviors of ultrafine-grained Cu-Zn alloy processed by equal-channel angular pressing," *Scripta Materialia*, Vol. 68, No. 6, 2013, pp. 389-392.

[11]   Singh, A., Tang, L., Dao, M., Lu, L., Suresh, S., "Fracture Toughness and Fatigue Crack Growth Characteristics of Nanotwinned Copper," *Acta Materialia*, Vol. 59, No. 6, 2011, pp. 2437-2446.

[12]   Watanabe, C., Monzen, R., Tazaki, K., "Effects of AL3Sc particle size and precipitate-free zones on fatigue behavior and dislocation structure of an aged Al-Mg-Sc alloy," *International Journal of Fatigue*, Vol. 30, No. 4, 2008, pp. 635-641.

[13]   Hansson, P., and Melin, S., "Dislocation-based modelling of the growth of a microstructurally short crack by single shear due to fatigue loading," *International Journal of Fatigue*, Vol. 27, No. 4, 2005, pp. 347-356.

[14]   Bjerkén, C., and Melin, S., "A Tool to Model Short Crack Fatigue Growth using a Discrete Dislocation Formulation," *International Journal of Fatigue*, Vol. 25, No. 6, pp. 559-566.

[15]   Larrouy, B., Villechaise, P., Cormier, J., Berteaux, O., "Grain boundary-slip bands interactions: Impact on the fatigue crack initiation in a polycrystalline forged Ni-based superalloy," *Acta Materialia*, Vol. 99, 2015, pp. 325-336

[16]   Kim, I. S., Choi, B. G., Jung, J. E., Do, J., Jo, C. Y., "Effect of Microstructural Characteristics on the Low Cycle Fatigue Behaviors of Cast Ni-base Superalloys," *Materials Characterization*, Vol. 106, 2015, Pages 375-381.

[17]   Zhang, P., Zhu, Q., Chen, G., Qin, H., Wang, C., "Grain Size Based Low Cycle Fatigue Life Prediction Model for Nickel-based Superalloy," *Transactions of Nonferrous Metals Society of China*, Vol. 28, No. 10, 2018, pp. 2102-2106.

[18]   Ostergen, W. J., "A Damage Function and Associated Failure Equations for Predicting Hold Time and Frequency Effects in Elevated Temperature Low Cycle Fatigue," *Journal of Testing and Evaluation*, Vol. 4, No. 5, pp. 327-339.

[19]   Salvat Cantó, J., Winwood, S., Rhodes, K., Birosca, S., "A Study of Low Cycle Fatigue Life and its Correlation with Microstructural Parameters in IN713C Nickel Based Superalloy," *Materials Science and Engineering: A*, Vol. 718, 2018, pp. 19-32.

[20]   Pineau, A., and Antolovich, S. D., "High Temperature Fatigue of Nickel-base Superalloys – A Review with Special Emphasis on Deformation Modes and Oxidation," *Engineering Failure Analysis*, Vol. 16, No. 8, 2009, pp. 2668-2697.

[21]   Arakere, N. K., and Swanson, G., "Effect of Crystal Orientation on Fatigue Failure of Single Crystal Nickel Base Turbine Blade Superalloys." *Journal of Engineering for Gas Turbines and Power,* Vol. 124, No. 1, 2000, pp. 161-176.

[22]   Cowles, B. A., "High Cycle Fatigue Failure in Aircraft in Aircraft Gas Turbines: An Industry Perspective," *International Journal of Fracture*, Vol. 80, 1996, pp. 147-163

[23]   Cervellon, A., Hémery, S., Kürnsteiner, P., Gault, B., Kontis, P., Cormier, J., "Crack Initiation Mechanisms during Very High Cycle Fatigue on Ni-based Single Crystal Superalloys at High Temperature," *Acta Materialia*, Vol. 188, 2020, pp. 131-144.

[24]   Hong, Y. and Sun, C., "The Nature and the Mechanism of Crack Initiation and Early Growth for Very-High-Cycle Fatigue of Metallic Materials – An Overview," *Theoretical and Applied Fracture Mechanics*, Vol. 92, 2017, pp. 331-350.

[25]   Blochwitz, C., Brechbühl, J., Tirschler, W., "Analysis of Activated Slip Systems in Fatigue Nickel Polycrystals using the EBSD-technique in the Scanning Electron Microscope," *Materials Science and Engineering: A*, Vol. 201, No. 1-2, 1996, pp. 42-47.

[26]   Charpagne, M. A., Stinville, J. C., Callahan, P. G., Texier, D., Chen, Z., Villechaise, P., Valle, V., Pollock, T. M. "Automated and Quantitative Analysis of Plastic Strain Localization via Multi-Modal Data Recombination," *Materials Characterization*, Vol. 163, 2020, 110245.

[27]   Shao, S., Khonsari, M. M., Guo, S., Meng, W. J., Li, N., "Overview: Additive Manufacturing Enabled Accelereated Design of Ni-based Alloys for Improved Fatigue Life," *Additive Manufacturing*, Vol. 29, 2019, 100779.

[28]   Yadollahi, A. and Shamsaei, N., " Additive Manufacturing of Fatigue Resistant Materials: Challenges and Opportunities," *International Journal of Fatigue*, Vol. 98, 2017, pp, 14-31.

[29]   Aramesh, M., Montazeri, S., Veldhuis, S. C., " A Novel Treatment for Cutting Tools for Reducing the Chipping and Improving Tool Life during Machining of Inconel 718," *Wear*, Vol. 414-415, 2018, pp. 79-88.

[30]   Wang, B., Zhang, Z. J., Shao, C. W., Duan, Q. Q., Pang, J. C., Yang, H. J., Li, X. W., Zhang, Z., "Improving the High-Cycle Fatigue Lives of Fe-30Mn-0.9C Twinning-Induced Plasticity Steel Through Pre-straining," *Metallurgical and Materials Transactions A*, Vol. 46, No. 8, 2015, pp. 3317-3323.

Figure A.1: Buehler Metaserv 250 Semiautomatic Twin Polisher.
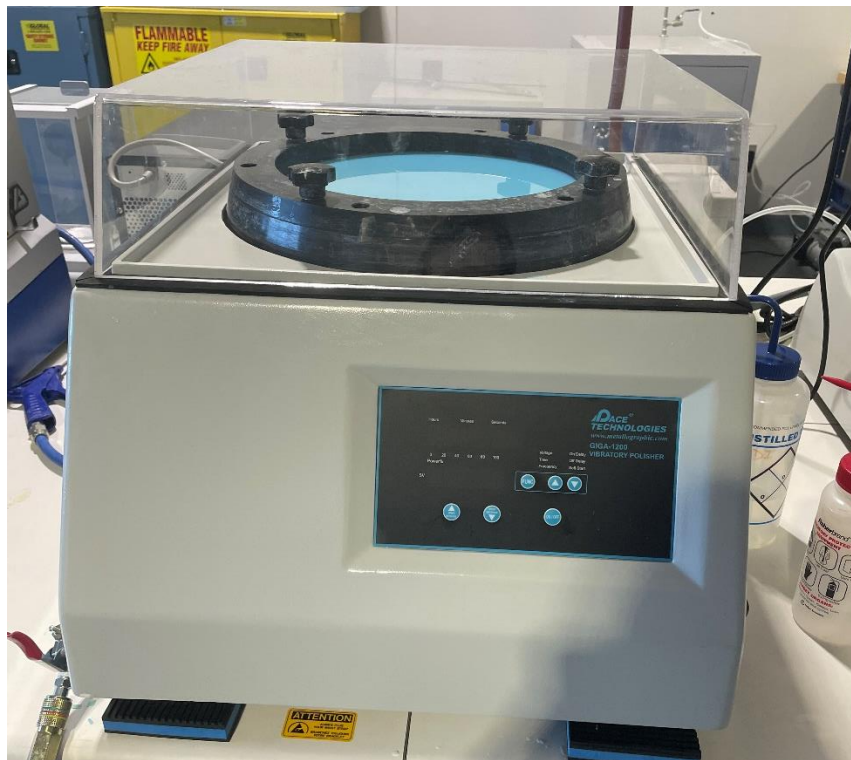

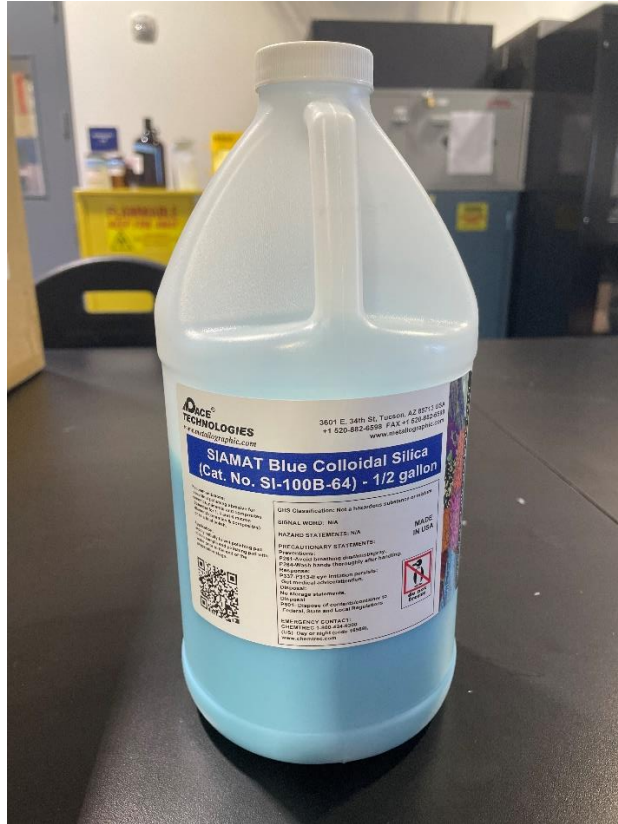*Figure A.2: Pace Technologies GIGA-1200 Vibratory Polisher.*

Figure A.3: Pace Technologies Blue Colloidal Silica.

Figure A.4: Branson Ultrasonic Cleaner.

Figure A.5: Wilson Tukon 1202 Micro-Hardness Tester.
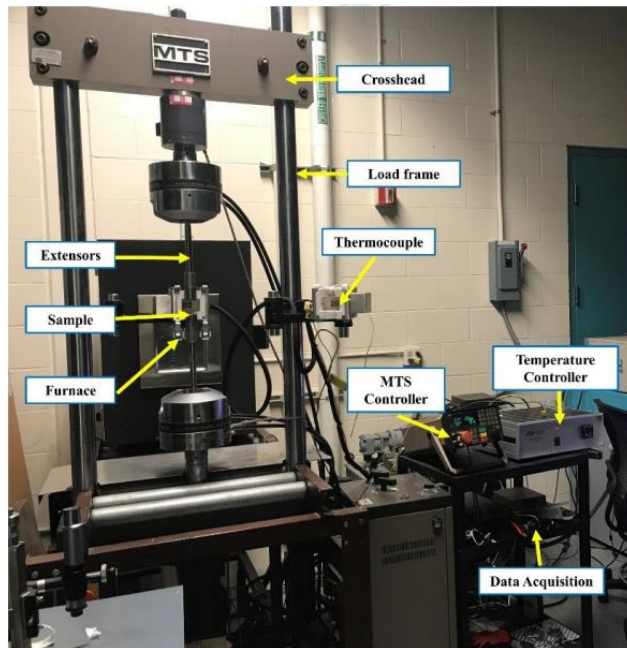

Figure A.6: MTS frame, furnace, and controller devices. [2]

MTS Applied Load Calculations

Sample 1 initial dimensions:
L: 20 mm W: 2.91 mm t: 1.19 mm
Sample 2 initial dimensions:
L: 20 mm W: 2.92 mm t: 1.22 mm

Given:
$\varepsilon = 1.0\% = 0.01$ mm/mm, E = 198 Gpa, $\sigma = 884$ Mpa

Sample 1 Input Load:
$P = \sigma * L * w$
$P = (884x10^6 \, Pa)(2.91x10^{-3} \, m)(1.19x10^{-3} \, m) =$
$P = 3061 \, N = 688 \, lb_f$

Sample 2 Input Load:
$P = \sigma * L * w$
$P = (884x10^6 \, Pa)(2.92x10^{-3} \, m)(1.22x10^{-3} \, m) =$
$P = 3149 \, N = 708 \, lb_f$

Input Loads with safety margin
Sample 1: 670 lb_f
Sample 2: 680 lb_f

Figure A.7: Hand calculations for MTS machine loads and applied stress.